Bioactive Materials 16 (2022) 451–471

Contents lists available at ScienceDirect

Bioactive Materials

journal homepage: www.keaipublishing.com/en/journals/bioactive-materials

Engineering an enthesis-like graft for rotator cuff repair: An approach to fabricate highly biomimetic scaffold capable of zone-specifically releasing stem cell differentiation inducers

Can Chen [a,b,c,d,k], Qiang Shi [b,c,d,e,k], Muzhi Li [b,c,d,f], Yang Chen [b,c,d,e,k], Tao Zhang [b,c,d,e,k], Yan Xu [b,c,d,e,k], Yunjie Liao [g], Shulin Ding [b,c,d,h], Zhanwen Wang [b,c,d,e,k], Xing Li [b,c,d,h], Chunfeng Zhao [i], Lunquan Sun [j], Jianzhong Hu [b,c,d,h,k,**], Hongbin Lu [b,c,d,e,k,*]

[a] Department of Orthopedics, Xiangya Hospital, Central South University, Changsha, 410008, China
[b] Key Laboratory of Organ Injury, Aging and Regenerative Medicine of Hunan Province, Changsha, 410008, China
[c] Hunan Engineering Research Center of Sports and Health, Changsha, 410008, China
[d] Xiangya Hospital-International Chinese Musculoskeletal Research Society Sports Medicine Research Centre, Changsha, 410008, China
[e] Department of Sports Medicine, Xiangya Hospital, Central South University, Changsha, 410008, China
[f] Department of Rehabilitation, The Second Xiangya Hospital, Central South University, Changsha, Hunan, 410011, China
[g] Department of Radiology, The Third Xiangya Hospital, Central South University, Changsha, 410013, China
[h] Department of Spine Surgery, Xiangya Hospital, Central South University, Changsha, Hunan, 410008, China
[i] Division of Orthopedic Research and Department of Orthopedic Surgery, Mayo Clinic, Rochester, Minnesota, 55905, United States
[j] Center for Molecular Medicine, Xiangya Hospital, Central South University, Changsha, 410008, China
[k] National Clinical Research Center for Geriatric Disorders, Xiangya Hospital, Central South University, Changsha, Hunan, 410008, China

ARTICLE INFO

Keywords:
Acellular matrix
Collagen-binding peptide
Stem cell differentiation inducer
Enthesis regeneration
Rotator cuff

ABSTRACT

Rotator cuff (RC) attaches to humerus across a triphasic yet continuous tissue zones (bone-fibrocartilage-tendon), termed "enthesis". Regrettably, rapid and functional enthesis regeneration is challenging after RC tear. The existing grafts bioengineered for RC repair are insufficient, as they were engineered by a scaffold that did not mimic normal enthesis in morphology, composition, and tensile property, meanwhile cannot simultaneously stimulate the formation of bone-fibrocartilage-tendon tissues. Herein, an optimized decellularization approach based on a vacuum aspiration device (VAD) was developed to fabricate a book-shaped decellularized enthesis matrix (O-BDEM). Then, three recombinant growth factors (CBP-GFs) capable of binding collagen were synthesized by fusing a collagen-binding peptide (CBP) into the N-terminal of BMP-2, TGF-β3, or GDF-7, and zone-specifically tethered to the collagen of O-BDEM to fabricate a novel scaffold (CBP-GFs/O-BDEM) satisfying the above-mentioned requirements. After ensuring the low immunogenicity of CBP-GFs/O-BDEM by a novel single-cell mass cytometry in a mouse model, we interleaved urine-derived stem cell-sheets into this CBP-GFs/O-BDEM to bioengineer an enthesis-like graft. Its high-performance on regenerating enthesis was determined in a canine model. These findings indicate this CBP-GFs/O-BDEM may be an excellent scaffold for constructing enthesis-like graft to patch large/massive RC tears, and provide breakthroughs in fabricating graded interfacial tissue.

1. Introduction

The rotator cuff (RC) consists of four entheses surrounding the proximal humerus and is critical for maintaining glenohumeral joint stability [1–3]. Histologically, these entheses are composed of triphasic yet continuous tissue zones: bony tissue with typical osteocytes, calcified and uncalcified fibrocartilage with aligned chondrocytes, and tendinous tissue with typical tenocytes [4–6]. Clinically, rotator cuff tear (RCT) is common, leading to substantial pain and disability of the upper extremity [1,7]. In recent years, improved arthroscopic

Peer review under responsibility of KeAi Communications Co., Ltd.
* Corresponding author. Xiangya Hospital, Central South University, No. 87, Xiangya Road, Changsha, 410008, Hunan, China.
** Corresponding author. Xiangya Hospital, Central South University, No. 87, Xiangya Road, Changsha, 410008, Hunan, China.
E-mail addresses: jianzhonghu@hotmail.com (J. Hu), hongbinlu@sina.com (H. Lu).

https://doi.org/10.1016/j.bioactmat.2021.12.021
Received 23 August 2021; Received in revised form 29 November 2021; Accepted 19 December 2021
Available online 5 January 2022

techniques have provided better results in the surgical management of RCT [2,8–10]. Unfortunately, the regenerated enthesis after RCT repair often exhibits disorganized fibrovascular scars without triphasic yet continuous structure, and rarely recovers the tissue toughness, thus predisposing the repaired RC enthesis to re-injury [11]. Hence, it is urgent to develop some adjuvant strategies to improve this clinical dilemma.

To solve this dilemma, many researchers have turned to develop a bioengineering enthesis-like construct [11–13], that can act as a biological patch even an in-vitro living construct to replace the damaged enthesis. To realize that, the biomimicry and bioactivity of scaffolds are deemed to be the most critical. To date, tissue engineers and biomaterial scientists have developed some scaffolds with bionic and functional characteristics using polymers (both natural and synthetic), ceramics or most commonly a combination of them (composites) [14]. However, these scaffolds are still not highly mimic normal enthesis in morphology and composition, at the same time, satisfying the adequate mechanical needs. Therefore, a simple strategy among tissue engineers is to use decellularized extracellular matrix as scaffolds that offer the advantage of great similarity with native enthesis tissue. The existing decellularization approaches were reported to decellularize a block of enthesis tissue derived from the insertions of Achilles tendon, anterior cruciate ligament, patellar tendon and RC [15,16], which successfully fabricated several kinds of decellularized enthesis matrix with large-size bulk shape. However, the chondrocytes of enthesis tissue are deeply enclosed in a dense and low-porous fibrocartilage [6,17], it is difficult for absolutely and rapidly removing these chondrocyte components from a block of enthesis tissue without jeopardizing its native extracellular matrix

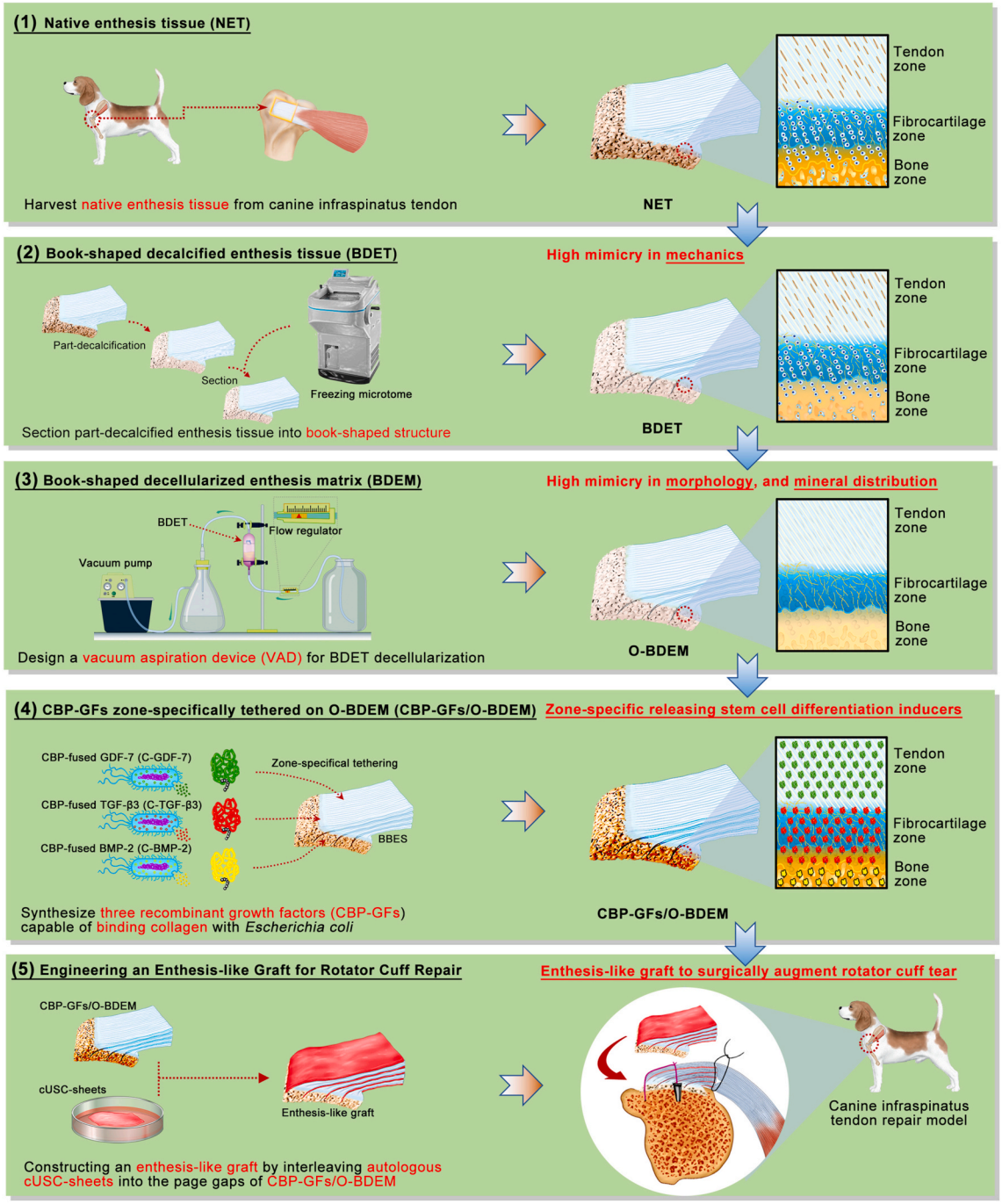

Fig. 1. Schematic illustration of the construction process of enthesis-like graft as well as its in vivo application.

integrity, especially for decellularizing large-sized enthesis tissue while well preserving its minor extracellular matrix components [18]. Moreover, the decellularized enthesis matrix was dense and compact with low porosity in microstructure, inconvenient for the endogenous cells migrating into its core [19], thus impeding new enthesis formation. The difficulty for endogenous cells migration may be more serious in large-sized decellularized enthesis matrix. In this study, using the book-shape slicing method described in our previous studies [20,21], large-sized enthesis tissue specimens were partly decalcified and sectioned into "book" shape along myotility direction with minimal influence to tensile resistance, and then decellularized within a custom-designed vacuum aspiration device (VAD) to acquire a book-shaped decellularized enthesis matrix (O-BDEM). This protocol exposed the chondrocytes deeply embedded in enthesis extracellular matrix to acellular reagents. More novelty, it provided a negative pressure environment to suck out cellular substances, thus quickly decellularizing enthesis while well reserving its extracellular matrix and tensile properties (Fig. 1).

During enthesis decellularization, some degree of damage to the enthesis extracellular matrix is always incurred [22]. Therefore, many researchers have explored the possibility of modifying or priming the decellularized enthesis matrix with growth factors (GFs) to restore the bioactivities damaged during the decellularization process. As for the bioactivities of decellularized enthesis matrix, the zone-specific inducibility of osteogenic, chondrogenic, and tenogenic lineages is one of the most critical aspect for enthesis regeneration [13]. Previous studies indicated that bone morphogenetic protein 2 (BMP-2), transforming growth factor β3 (TGF-β3), and growth differentiation factor 7 (GDF-7) respectively showed superior performance in inducing stem cells toward osteogenic, chondrogenic, and tenogenic lineages [13,23–25], implying that BMP-2, TGF-β3, and GDF-7 are suitable for improving the function of decellularized enthesis matrix in RC enthesis regeneration. Generally, the common strategy for GFs introduction into scaffolds is direct protein incorporation; However, the directly incorporated GFs diffuse and degrade too rapidly, making the local environment around the implanted scaffold in a state of high GFs at the early phase, thus delivering some undesirable side-effects [26,27]. To solve this problem, chemical cross-linking was developed to retain GFs on the scaffold, but which would affect its bioactivity and the structure of scaffold [28]. Another attractive strategy is the encapsulation of GFs into microspheres or nanoparticles that can be incorporated into the scaffold during the production phase. The use of such particles enables synchronization of release kinetics with material carrier degradation rate, allowing for extended and/or sequential GFs release [29]. However, this approach is not suitable for natural biomaterials like acellular matrix. During the hemostasis of vessel injury, a hemostasis factor, named as von Willebrand factor (vWF), was found to initiate the thrombosis cascade by specially binding to collagen beneath the endothelial cells [30]. Several studies determined that the A3 domain, also called collagen-binding peptide (CBP) plays a vital role in binding collagen [31,32]. Enlightened by this, we fused the CBP into the N-terminal of BMP-2, TGF-β3, or GDF-7 to synthesize three recombinant growth factors (CBP-GFs) capable of binding collagen, namely CBP-fused BMP-2 (C-BMP-2), CBP-fused TGF-β3 (C-TGF-β3) and CBP-fused GDF-7 (C-GDF-7). As collagen is the main component of O-BDEM, we respectively tethered the three CBP-GFs to the bony, fibrocartilaginous, and tendinous zone of O-BDEM to construct a novel scaffold, namely CBP-GFs zone-specifically tethered O-BDEM (CBP-GFs/O-BDEM), which satisfies the requirements in both biomimetic properties and zone-specific release of stem cell differentiation stimulators (Fig. 1). As a scaffold suitable for clinical translation and application, it must show good cytocompatibility and immunogenicity in-vivo [33]. Herein, a novel technique, single-cell mass cytometry (CyTOF) [34], was used to reveal the immunological response of CBP-GFs/O-BDEM at single-cell resolution using a mouse model.

The source of stem cell is another critical component for bioengineering the required enthesis-like graft. Preclinical and clinical studies have determined that the mesenchymal stem cells (MSCs) derived from bone marrow, adipose tissue, synovium and tendon, has the therapeutic potential for enthesis regeneration [35,36]. However, these type of MSCs are restricted by the invasive and painful harvesting procedures, which may cause donor site morbidity and limit their use for autogenous approaches. Recently, urine-derived stem cells (USCs) have attracted significant attention and been studied as a promising cell source by tissue engineers owning to their multilineage potential and sufficient proliferation capacities [37,38]. The advantages of USCs include noninvasive and low expense harvesting. Most importantly, USCs can be conveniently isolated from autologous urine, thus did not induce immune responses or rejection after in-vivo application, which was very ethical at autologous application [38,39]. In this study, USCs were isolated and cultured to form urine-derived stem cell-sheets (USC-sheets), and then interleaved into the page gap of CBP-GFs/O-BDEM to engineer a novel enthesis-like graft (Fig. 1). The in-vivo function of this enthesis-like graft in RC enthesis regeneration was elucidated using a preclinical canine model.

2. Materials and methods

2.1. Study design

The Animal Ethics Committee of Central South University (AEC-CSU) (No. 2019030517) approved the experimental procedures and animal care for the use of C57BL/6 mice (8-week-old) and adult male beagle dogs (8-month-old) in this study. The objectives of this study were to fabricate a scaffold (CBP-GFs/O-BDEM) satisfying the requirement in high biomimicry and zone-specific release of stem cell differentiation inducers, and then engineer an enthesis-like graft for patching RC tear. Firstly, we established a protocol for fabricating CBP-GFs/O-BDEM, and then systematically evaluated its following properties: (i) similarity to the native enthesis in morphology, ingredients, and tensile resistance; (ii) zone-specific differentiation inducibility for stem cells. Secondly, for evaluating the low immunogenicity of the CBP-GFs/O-BDEM, the mouse with right supraspinatus tendon injury were patched with different dispose: acellular human dermal matrix (AHDM) (n = 9, as positive control), CBP-GFs/O-BDEM (n = 9), and direct suture (CTL) (n = 9, as negative control). At postoperative 21-day, the blood from the mice was pooled for systemically analyzing immune cell activation at the single-cell level using CyTOF. Local immunological response to CBP-GFs/O-BDEM implantation was also evaluated with hematoxylin and eosin (H&E) staining and immunofluorescence. Lastly, we engineered an enthesis-like graft by interleaving the autogenous USC-sheets with CBP-GFs/O-BDEM, and elucidate its *in-vivo* function on RC enthesis regeneration using a canine infraspinatus tendon repair model. A total of 26 dogs were operated and augmented with or without an implant, and all of them reached endpoints (n = 13 for control; n = 13 for treated). Power analysis was performed before this preclinical canine study to determine the sample size.

2.2. Screening of the layer thickness for sectioning enthesis tissue into "book" shape

Canine infraspinatus tendon with bony attachment was harvested from dogs sacrificed in the local slaughterhouse, and the acquired native enthesis tissue (NET) specimens were carefully trimmed to cuboid shape (about 30 mm × 10 mm × 3 mm). After washing with 1% penicillin-streptomycin-amphotericin B solution (03-033-1B, BioInd, Israel) under a sterile environment using high-pressure water jet to wash out the marrow, the tendinous and fibrocartilaginous regions of these NET specimens were wrapped by Parafilm avoiding the influence of decalcification solution. Decalcification solution contains 10% EDTA, 1% penicillin-streptomycin-amphotericin B solution, protease inhibitor (1 tablets/100 mL, S8820-20TAB, Sigma). After that, these NET specimens

were partly decalcified at 4 °C for 3–5 days in a sterile environment, and then vertically sliced at the interfacial tissue between fibrocartilage and tendon (Fig. S1A). The sections stained with Masson's trichrome (MT) were used to calculate the mean diameters of the tertiary fiber bundle (Fig. S1A). According to this mean diameter, the decalcified enthesis tissue specimens were sliced into "book" shape from the tendinous end to bony end parallel to myotility direction with layer thicknesses of 150, 200, 250, or 300 μm, and then trimmed into a rectangle with the same cross-sectional area (8.0 mm^2). Meanwhile, the decalcified enthesis tissue specimens were also trimmed into a rectangle with a cross-sectional area of 8.0 mm^2. After these specimens were lyophilized, the bony and tendinous ends of the NET or book-shaped decalcified enthesis tissue (BDET) embedded with resin were fixed into the grip of the mechanical testing system (MTS Systems Corp, USA) for biomechanical test (Fig. S1B). Each specimen was preloaded to 1 N and then pulled to failure at a rate of 10 mm/min. Failure load and stiffness were calculated from the load-displacement curve obtained during the test.

2.3. Fabrication of book-shaped decellularized enthesis matrix (BDEM)

During decellularization, all of the procedures were performed in a clean bench, 1% penicillin-streptomycin-amphotericin B solution were supplemented into the aforementioned solutions, and protease inhibitor (1 tablets/100 mL, S8820-20TAB, Sigma) was supplemented into all solutions except the nuclease solution. Based on the above study, layers 250 μm in thickness were selected for preparing a BDET. Then, the BDET specimens were immersed in 30 mL 0.9% PBS and then sealed in a 50 mL sterile centrifuge tube. For the procedure of freezing, we directly immersed the tube into liquid nitrogen for 2 min. For the procedure of thawing, we directly immersed the frozen tube into water bath set at 37 °C for 10 min, which ensured that the 30 mL 0.9% PBS in the tube was always in the state of ice or ice water mixture, thus keeping the specimens in a low temperature state. After that, the specimens were rinsed with PBS for three times (0.5 h each). As for the conventional protocol [40,41], the specimens were digested with nuclease solution at 37 °C for 12 h (100 μg/mL RNase + 150 IU/mL DNase) followed by PBS rinsing for three times (0.5 h each). As for the optimized protocol, the specimens were digested with nuclease solution (100 μg/mL RNase + 150 IU/mL DNase) at 37 °C for 1 h followed by PBS flowing rinsing in a VAD (0.08 mPa negative pressure) for 0.5 h, and repeated this procedure for 1, 2, 3, or 4 times to screen an optimized protocol for BDET decellularization (Figure S2 and Move S1). NET or BDEM prepared by rinsing in a VAD for 1, 2, 3, or 4 times was stained with 4',6-diamidino-2-phenylindole (DAPI) for observing the retention of nuclear materials. Meanwhile, DNeasy Blood&Tissue Kit (Qiagen, USA) together with PicoGreen DNA assay kit (Invitrogen, USA) was used to quantify their DNA content. The minimum times of rinsing in VAD was selected as the optimized protocol for fabricating O-BDEM.

Supplementary video related to this article can be found at https://doi.org/10.1016/j.bioactmat.2021.12.021

2.4. Histological evaluation of BDEM

BDET was decellularized by a conventional protocol (by Liu Q) [40,41], or our optimized protocol, thus acquiring two kinds of BDEM (respectively named as C-BDEM or O-BDEM). NET, C-BDEM, or O-BDEM was embedded in paraffin and sliced with 5 μm thickness, then staining with Hematoxylin & eosin (H&E) or DAPI for observing the retention of nuclear materials. Meanwhile, we used DNeasy Blood&Tissue Kit (Qiagen, USA) together with PicoGreen DNA assay kit (Invitrogen, USA) to quantify their DNA content. As for evaluating the preservation of collagen and proteoglycans in the NET, C-BDEM, or O-BDEM, paraffin embedded NET or BDEM were sagittally sliced with 5 μm thickness, and then rapidly spread on a BaF_2 substrate. After dewaxing, the sections were dried overnight under vacuum and then scanned with synchrotron radiation-Fourier transform infrared spectroscopy (SR-FTIR) (BL01B beamline, National Facility for Protein Science Shanghai and Shanghai Synchrotron Radiation Facility, China) to capture the infrared spectrum. The peak area of amide I (1720-1590 cm^{-1}) and carbohydrate (1140-985 cm^{-1}) in the infrared spectrum were respectively calculated to characterize the distribution and content of collagen and proteoglycans in the NET, C-BDEM, or O-BDEM according to pervious literature [36]. Additionally, the adjacent sections were stained with sirius red (SR) or toluidine blue (TB) for observing the distribution of collagen and proteoglycans in the scaffolds. Furthermore, the mechanical properties of the NET, C-BDEM, or O-BDEM were comparatively evaluated with mechanical testing system (MTS Systems Corp, USA) with the above-mentioned protocol.

2.5. SDS-PAGE and mass spectrometry

NET, C-BDEM, or O-BDEM specimens (n = 3) were snap-frozen in liquid nitrogen for protein extraction as described before [42]. Proteins extracted from NET, C-BDEM and O-BDEM (n = 3/group) were loaded into 8–16% sodium dodecyl sulfate-polyacrylamide gel (No. 456-8104, Bio-Rad) and separated by electrophoresis. 10 μg of total protein was loaded into each well of the polyacrylamide gel. The polyacrylamide gel was then stained with Imperial™ Protein Stain for visualization (No. 24615, Thermo Scientific).

NET, C-BDEM and O-BDEM (n = 3/group) were first homogenized and sonicated in radioimmunoprecipitation assay (RIPA) buffer, and then spun down to collect supernatant. After dealt with chloroform/methanol/water protein precipitation following by twice washing, the collected protein pellet was solubilized in Rapigest, and then treated with DTT/IAN followed by Lys-C/Trypsin digestion. Samples were quantified using a Nanodrop and analyzed by a microcapillary tandem mass spectrometry (LC-MS/MS) Q-Exactive Plus system with long gradient for label-free quantification. After processing the acquired proteomics data with Progenesis QI software, the subcellular location of each identified canine protein was determined using the Universal Protein Knowledge Base (UniProtKB, www.uniprot.org). ECM proteins were identified by querying the lists of unique proteins in NET, C-BDEM, or O-BDEM with the UniProt database for the subcellular location search terms "extracellular" combined with the cellular component search terms "extracellular zone" by the Gene Ontology Consortium [43,44]. Protein abundance in NET, C-BDEM and O-BDEM specimens were calculated from the lg LFQ intensity.

2.6. Evaluating the minerals distribution and content of O-BDEM using synchrotron radiation-based micro X-ray fluorescence (SR-μXRF)

Calcium (Ca) and phosphorus (P) are the two essential elements for generating hydroxyapatite (HA) crystallites, which participate in the biomineralization process by depositing into the extracellular matrix of hard tissue [45]. Thus, the contents of the two elements were used as a parameter to describe the mineral level in O-BDEM. To evaluate the Ca and P distribution and content in O-BDEM, it was embedded within polymethylmethacrylate (PMMA) and sectioned into 100 μm slices by a microtome (EXAKT 300CP; Germany) and grinding machine (EXAKT400CS; Germany). The Ca and P at the O-BDEM were detected by Synchrotron radiation-based micro X-ray fluorescence (SR-μXRF) at BL15U1, Shanghai Synchrotron Radiation Facility, China [45], where synchrotron radiation (SR) X-rays were focused to a size of 8 μm × 6 μm (horizontal × vertical) by a K–B mirror pair (Xradia Inc.). The slice was fixed to the platform at a 45° angle to the SR X-ray beams, and a silicon drift detector (SSD) (Vortex, USA) was placed at a 90° angle to the SR X-ray beams to collect the fluorescent counts of target elements. Incident SR X-rays of 10 keV were used to stimulate the samples. The specimens were fixed to a sample platform controlled by a motorized X–Y mapping stage and were continually scanned in steps of 7 μm × 5 μm (horizontal × vertical). The SR-μXRF maps were acquired from the ROI with a resolution of 7 μm × 5 μm for 1 s/pixel, showing the distributions of Ca and

P contents at the scaffold.

2.7. Preparation of CBP-GFs or GFs and its function evaluation

The C-BMP-2, C-TGF-β3, or C-GDF-7 consists of a 6 × His tag, a collagen binding peptide (CBP) (WREPSFCALS), a linker sequence (GSAGSAAGSGG) and the N-terminus of the mature human GFs fragment, while the BMP-2, TGF-β3 and GDF-7 did not include CBP (Table S1). The gene of BMP-2, C-BMP-2, TGF-β3, C-TGF-β3, GDF-7, and C-GDF-7 was respectively inserted into the pET30a vector (Novagen, Madison), and then transformed into BL21 strain of *Escherichia coli*. The expressed proteins by *Escherichia coli* were purified with the help of 6 × His tag, and then identified by SDS-PAGE together with western-blotting with anti-6 × His tag antibody (Sigma).

USCs from human (hUSCs) were isolated according to the pervious protocol [46]. The isolated cells were identified by flow cytometry using antibodies (CD29, CD44, CD90, CD105, CD73, CD11b, CD34, and CD45) (Table S2). Besides, osteogenic, chondrogenic, and adipogenic differentiation potential of isolated cells were also evaluated in-vitro to further identify hUSCs. Passage 2 cells were used for the following experiments.

Osteogenic inducibility of C-BMP-2 and BMP-2, chondrogenic inducibility of C-TGF-β3 and TGF-β3, as well as tenogenic inducibility of C-GDF-7 and GDF-7 was measured with hUSCs (10^4 cells/well in 48-well plates). According to literatures [47–49], 1 μg/mL C-BMP-2, 1 μg/mL BMP-2, 10 ng/mL C-TGF-β3, 10 ng/mL TGF-β3, 10 ng/mL C-GDF-7 or 10 ng/mL GDF-7 was respectively added into the culture medium. After 3 days culture, cellular immunofluorescent assay was used to evaluate the expression of Runx2, Sox9 and Scx. Meanwhile, the expression of osteogenic (Runx2, Ocn), chondrogenic (Sox9, Acan) and tenogenic (Scx, Tnmd) genes was determined using qRT-PCR. The primer sequences for these genes are provided in Table S3. Housekeeping gene (GAPDH) was used for normalization. The results are shown as fold change related to the hUSCs in the tissue culture polystyrenes (TCPS) (as control group).

2.8. Binding assays of CBP-GFs in-vitro

According to the previous literatures [50,51], the binding assays of CBP-GFs were evaluated by a modified ELISA method. In brief, O-BDEM was carefully cut into a decellularized bony matrix (DBM), decellularized fibrocartilaginous matrix (DFM), or decellularized tendinous matrix (DTM), respectively; then, equimolar amounts of BMP-2 or C-BMP-2, TGF-β3 or C-TGF-β3, and GDF-7 or C-GDF-7 with gradient concentrations (2 μM, 4 μM, 6 μM, 8 μM, 10 μM, 12 μM) were respectively added to the DBM, DFM, and DTM with 12 h incubation at 4 °C. After washing three times, the primary antibody (1:1000, anti-6 × His tag antibody, Sigma) was incubated with the three kinds of scaffold for 1 h at 37 °C. After washing again, secondary antibody (1:10000, AP-conjugated anti-mouse IgG antibody, Sigma) was incubated for 1 h at 37 °C. After washing, P-NPP disodium (2 mg/mL) was added for 10min at room temperature (RT), and the reaction was terminated by 0.2 M NaOH. The binding curve was drawn by the absorbance at 405 nm measured using a microplate reader.

2.9. Sustained release assays of CBP-GFs from CBP-GFs/O-BDEM in-vitro

To evaluate the sustained release of GFs from CBP-GFs/O-BDEM *in-vitro*, 8 μM BMP-2 or C-BMP-2, 6 μM TGF-β3 or C-TGF-β3, 8 μM GDF-7 or C-GDF-7 were respectively tethered into the DBM, DFM, or DTM for 12 h incubation at 4 °C, and then transferred into 24-well plate. Subsequently, 1 mL PBS (pH = 7.4) was added to each well, and then the plate was horizontally shaken with a speed of 80 rpm at 37 °C to simulate the flow of body fluid. The added PBS was replaced every 24 h, the residual BMP-2 or C-BMP-2, TGF-β3 or C-TGF-β3, and GDF-7 or C-GDF-7 in scaffold was measured from day 0 to day 10 using the above-mentioned modified ELISA method. Briefly, the primary antibody (1:1000, anti-6 × His tag antibody, Sigma) was incubated with the scaffold for 1 h at 37 °C. After washing, secondary antibody (1:10000, AP-conjugated anti-mouse IgG antibody, Sigma) was incubated for 1 h at 37 °C. After washing, P-NPP disodium (2 mg/mL) was added for 10min at room temperature (RT), and the reaction was terminated by 0.2 M NaOH. A microplate reader was used to measure the absorbance at 405 nm from day 0 to day 10. The absorbance at 405 nm from day 1–10 were respectively divided by the absorbance at 405 nm at day 0, and the acquired values were used to draw the releasing curve.

C-BMP-2 or BMP-2 labeled with Alexa Fluor™ 405 Antibody Labeling Kit (ThermoFisher scientific, USA), C-TGF-β3 or TGF-β3 labeled with Alexa Fluor™ 488 Antibody Labeling Kit (ThermoFisher scientific, USA), C-GDF-7 or GDF-7 labeled with Alexa Fluor™ 594 Antibody Labeling Kit (ThermoFisher scientific, USA) were spatially bound to the bony zone, fibrocartilaginous zone and tendinous zone of O-BDEM, respectively. After incubation at 4 °C for 12 h, the CBP-GFs/O-BDEM or NAT-GFs/O-BDEM were transferred to 48-well plate. And then, 500 μL PBS was added to each well. The plate was incubated on a rocker platform (80 rpm, 37 °C) to simulate the flow of body fluid, and the added PBS were replaced every 24 h. The scaffolds were collected at day 0, 1, 4, 7 or 10 to observe the spatial retention of CBP-GFs or NAT-GFs on the O-BDEM using a fluorescence microscope.

2.10. Spatial inducibility of CBP-GFs/O-BDEM on stem cell differentiation

O-BDEM were carefully cut into an DBM, DFM, and DTM, then 8 μM BMP-2 or C-BMP-2, 6 μM TGF-β3 or C-TGF-β3, 8 μM GDF-7 or C-GDF-7 were respectively tethered into the DBM, DFM, or DTM to acquire BMP-2/DBM, C-BMP-2/DBM, TGF-β3/DFM, C-TGF-β3/DFM, GDF-7/DTM, C-GDF-7/DTM. After that, the DBM, DFM, and DTM were closely placed together in a culture dish, the BMP-2/DBM, TGF-β3/DFM, and GDF-7/DTM were also closely placed together in another culture dish, the C-BMP-2/DBM, C-TGF-β3/DFM, and C-GDF-7/DTM were also closely placed together in another culture dish. After seeding 2 × 10^6 hUSCs on these scaffolds, the expression of osteogenic (Runx2, Ocn), chondrogenic (Sox9, Acan), tenogenic (Scx, Tnmd) specific genes in hUSCs were evaluated by qRT-PCR after 5-day culture. The primer sequences for these genes are provided in Table S3. Housekeeping gene (GAPDH) was used for normalization. The results are shown as fold change related to the hUSCs in the TCPS group. The expressions of Runx2, Sox9 and Scx in the hUSCs after 5-day culture was evaluated by immunofluorescence assay to assess the spatial inducibility of scaffold using anti-Runx2 antibody, anti-Sox9 antibody, and anti-Scx antibody. Meanwhile, anti-collagen II antibody was used to label collagen II.

2.11. Inflammatory responses of CBP-GFs/O-BDEM in a murine model

In order to systematically evaluate the inflammatory responses between the host and implants, CyTOF, the latest technique in flow cytometry, was performed for analyzing the murine blood to characterize the CBP-GFs/O-BDEM-induced systemic inflammatory responses in a supraspinatus tendon repair model. Meanwhile, local inflammatory responses induced by the CBP-GFs/O-BDEM were also evaluated by analyzing the infiltration of neutrophils (Ly6g) and macrophages (F4/80) at the site of implantation with immunofluorescence. Briefly, one layer of CBP-GFs/O-BDEM was cut into 5 × 2 × 0.25 mm^3 for surgical implantation, and the clinical approved AHDM with similar size was also implanted as reference. A total of 27 mouse were anesthetized with pentobarbital sodium (8 mg/mL, 0.1 mL/10g), and randomly allocated to three group patched with different treatments: CBP-GFs/O-BDEM (n = 9), AHDM (n = 9) and control group (CTL) (n = 9). In order to expose the supraspinatus tendon, we made a longitudinal skin incision on the anterolateral side of the left shoulder, and then transversely split the

deltoid muscle. After we used a 1 ml syringe needle to punch the supraspinatus tendon insertion, a CBP-GFs/O-BDEM or AHDM was used to cover the injured supraspinatus tendon insertion. And then, a PDS suture (6-0, Ethicon, USA) was sequentially passed through the myotendinous junction of supraspinatus tendon and the tendinous end of CBP-GFs/O-BDEM or AHDM to suture them together. Meanwhile, another PDS suture was sequentially passed through the greater tuberosity of humerus and the bony end of CBP-GFs/O-BDEM or AHDM to fix them together. Finally, the overlying deltoid muscle and skin were closed, and the mice were allowed to engage in free cage activity.

At postoperative 21 days, the blood pooled from three mice in each group was mix together as one sample to obtain sufficient cells for a reliable mass cytometry. After lysis of the red blood cells, samples were washed using FACS buffer and stored at 4 °C. And then, we stained the pooled cells with cisplatin for isolating live cells and dead cells. After blocking the cells at RT for 20 min, they were stained with a mixture of metal-tagged antibodies binding the surface antigens for 0.5 h at RT (the antibodies were provided in Table S4). After washing the cells with FACS buffer, they were fixed for 0.5 h at RT, and then stained with DNA intercalator overnight at 4 °C. Following this, the cells were washed with Perm buffer, and then incubated with barcodes at 4 °C for 0.5 h. After washing the cells with ACS buffer and ultrapure H_2O, a CyTOF machine were used to analyze them. The acquired raw data was uploaded to a Cytobank web server (Cytobank Inc.) for further data processing. In this study, we analyzed at least 35,000 live single cells in each sample.

The gated live cells were analyzed with SPADE algorithms with the target number of nodes set to 200 in Cytobank. In SPADE algorithms, the color gradient represents the median expression level of the chosen marker. Herein, we selected the following markers for immune-related clustering: CD45, F4/80, CD11b, CD11c, CD4, CD8, CD49b, Ly6G, Ly6C, B220, TCRγδ and CD3. Based on marker expression, we defined immune cell populations in the mice blood samples, including neutrophil ($CD45^+CD11b^+Ly6g^+$), macrophage ($CD45^+CD11b^+F4/80^+$), monocyte ($CD45^+CD11b^+Ly6c^+$), dendritic cells (DC cells) ($CD45^+CD11b^+CD11c^+$), NK cells ($CD45^+CD11b^+CD49b^+$), $CD4^+$T cells ($CD45^+CD3^+CD4^+$), $CD8^+$T cells ($CD45^+CD3^+CD8^+$), γδT cells ($CD45^+CD3^+TCRgd^+$), B cells ($CD45^+B220^+$). The proportion of each immune cell population was calculated for each defined population out of the total immune cells. Intensity levels of markers were calculated on transformed median intensity values in each defined cell population.

After the mice were sacrificed at postoperative 21-day, we macroscopically evaluated the implant residuals at the implanted site, and then subsequently subjected to H&E staining. Considering that neutrophils and macrophages are the predominant contributors to forming fibrotic capsule [52], we examined the infiltration of neutrophils (Ly6g) and macrophages (F4/80) at the implant site using immunofluorescence assay. The neutrophils and macrophages were detected with anti-bodies of mouse Ly6g (127601, Biolegend) and mouse F4/80 (ab100790, Abcam).

2.12. Constructing enthesis-like graft

C-BMP-2 solution (8 μM), C-TGF-β3 solution (6 μM), C-GDF-7 solution (8 μM) were respectively immersed into the bone zone, fibrocartilage zone, and tendon zone of O-BDEM with the help of a custom-designed setup, thus zone-specifically tethering CBD-GFs into O-BDEM to fabricate a CBP-GFs/O-BDEM.

After the dog was anesthetized with 3% pentobarbital sodium (0.15 ml/kg), we obtained about 20 mL of urine sample from each dog three weeks prior to surgery with a sterile catheter. After the urine sample was centrifugated at 400×*g* for 10 min, we discarded the supernatant and collected the residual urine sample (about 1 mL) left in the tube. After 10 mL PBS was added to the tube, we gently resuspended the cell pellets deposited at the bottom of the tube. After the urine sample was centrifugated at 200×*g* for 10 min, we discarded the supernatant to collect the cell pellets in the tube. After that, we resuspended the cell pellets with 3 mL primary medium, and averagely transferred into two wells of a 12-well plate. The isolated cells were incubated at 37 °C containing 5% CO_2. After 2-day, 1 mL primary medium was directly added to the culture without removing any medium. After 4-day, 1 mL medium was removed and 1 mL proliferation medium was added. Thereafter, the whole medium was changed with proliferation medium every other day. The colonies of isolated cells were captured by an inverted microscope (Leica DMI6000B, Solms, Germany). Cells were passaged at 80–90% confluence. Primary medium contains DMEM/F-12 supplemented with the REGM SingleQuot kit (Lonza, USA), 10% fetal bovine serum (FBS; Gibco) and 1% Antibiotics (Gibco, Grand Island, USA). Proliferation medium contains mixed (1:1 ratio) DMEM/F-12 and RE basal medium (RBM) supplemented with the REGM Bullet Kit (Lonza), 10% FBS (Gibco), 1% Antibiotics (Gibco), 1% GlutaMAX (Gibco), 1% NEAA (Gibco), 5 ng/mL bFGF (Peprotech, USA), 5 ng/mL PDGF-BB (Peprotech) and 5 ng/mL EGF (Peprotech).

Canine USCs (cUSCs) were identified by flow cytometry using antibodies (CD29, CD44, CD90, CD105, CD11b, CD34, and CD45) (Table S2). Besides, multi-lineage differentiations (including osteogenesis, adipogenesis and chondrogenesis) of the isolated cells were also evaluated with Alizarin Red S staining (at day 21), Oil Red O staining (at day 21) and Alcian Blue staining (at day 21) to further identify cUSCs, respectively.

cUSC-sheet was fabricated using a method described in previous literature [36]. In brief, cUSCs (2×10^6, passage 2) were cultured on temperature-responsive dishes (6 cm diameter, UpCell, ThermoFisher Scientific, USA) in complete medium added 20 μg/mL L-ascorbic acid (Sigma, USA) to induce cell-sheet formation. Medium was replaced every two days. After the cUSC-sheets were spontaneously detached from the culture dishes, the stemness of cUSCs in cell-sheet was evaluated using trilineage differentiations. Then, three slices of cUSC-sheets were separately interleaved into the page gaps of CBP-GFs/O-BDEM, and then the other two slices of cUSCs-sheet were used to cover the top and bottom surfaces of the CBP-GFs/O-BDEM for bioengineering an enthesis-like graft (Movie S2). The constructed enthesis-like graft was evaluated by gross observation and subsequent H&E staining.

Supplementary data related to this article can be found at https://doi.org/10.1016/j.bioactmat.2021.12.021.

2.13. Surgical processes of canine infraspinatus tendon repair model

As shown in Fig. S3, after anesthesia, the right shoulder of the dog was shaved and sterilized. A 5-cm curved incision was made at the anterolateral margin of the humerus to expose the lateral margin of the deltoid muscle. After separating the lateral space of the deltoid muscle, the infraspinatus tendon was exposed. The infraspinatus tendon was then completely detached from its insertion at the greater tuberosity of humerus. The residual fibrocartilage at the insertion was ground off to expose the underlying bone marrow. In the CTL group (Fig. S3A), the infraspinatus tendon end was anatomically sutured to its original footprint using Suture Anchor, Bio-FASTak (AR-1324BF, Arthrex, Naples, Germany). Briefly, after two bony tunnels were made at the greater tuberosity with a 1-mm-diameter drill bit, two medial anchors were inserted into the upper and lower poles of the footprints at a 4-mm distance. After one suture limb from one anchor was passed through the infraspinatus tendon end, it was again passed through the infraspinatus tendon end from the outer surface to the inner surface anterolaterally. Thus, a loop was formed on the outer surface of the infraspinatus tendon end. This limb passed then through the infraspinatus tendon end from the inner surface to the outer surface anteromedially. Another suture limb was then passed through the infraspinatus tendon end from the inner surface to the outer surface anteromedially, and across the loop to create a rip-stop. After knotting the two suture limbs, one limb was parallelly passed through the bone cortex of the lateral margin of the footprints and knotted with the other suture limb to ensure that the tendon end firmly fit the upper or lower

part of the footprint area. The sutures from the other anchor perforated the infraspinatus tendon end with a same way. To make the tendon end closely fit with the middle part of the footprint area, two suture limbs from the two different anchors were tightly knitted together. Additionally, the suture was strengthened by Kessler repair using the other two limbs. In the EG group (Fig. S3B), two medial anchors were similarly inserted into the same position as the CTL group. Two suture limbs from one anchor were respectively passed through the predrilled tunnels on the bony zone of EG graft and then knotted together to fix the bony end of the EG graft to the footprint area. Then, one limb from one anchor was parallelly passed through the bone cortex of the lateral margin of the footprints and knotted with another limb to ensure that the bony part of the EG graft firmly fit the footprint area. After the infraspinatus tendon end was cut horizontally into two layers, one suture limb was passed through the tendon end with a Kessler repair to pull the tendon end to the footprint area and to avoid excessive tension focused on the implant in the early phase. The tendinous part of the EG graft was then sandwiched by the split infraspinatus tendon ends and the edges of this sandwiching construct were sutured together with continuous 5-0 PDS sutures (Ethicon). After closing the surgical incision, the dogs were allowed free cage activity with a cast immobilization to avoid excessive weight bearing and separation of the junction reattachment (Fig. S3C). Painkillers (tramadol; Grunenthal GmbH) were administered postoperatively for seven days (P.O, q8h, 50 mg). Amoxicillin and clavulanate potassium tablets (Zhuhai united laboratories Co. Ltd, China) were administered as prophylactic antibiotics for 5 days (P.O, q12h, 475 mg).

2.14. MRI scanning and quantitative measurement

Dogs (n = 5/group) were anesthetized with 3% pentobarbital sodium (0.2 ml/kg), and then received clinical MRI examination (Ingenia 3.0T MR system; Philips, Germany) for imaging infraspinatus tendon enthesis. Dog was laid in a supine position with both upper limbs perpendicular to the chest (Fig. S4A). The body surface coil was closely put on their surface of shoulders. The oblique axial images were acquired through the long axis of the infraspinatus tendon with scanning parameters (Fig. S4B).

The signal-to-noise quotient (SNQ) of the repair tissue was used as parameters for quantitative measurement of RC healing [53], which was calculated according to the following equation: SNQ = (Signal intensity of the repaired infraspinatus tendon insertion - Signal intensity of native infraspinatus tendon insertion)/Signal intensity of background. The region of interest (ROI) used to measure the signal intensity of the repaired infraspinatus tendon insertion, which was defined according to the surgical repaired tissue area on MRI images (Fig. S4C). Meanwhile, the ROI of background was located approximately 3 cm anterior to the infraspinatus tendon. Additionally, the ROI of native infraspinatus tendon enthesis was circled on its interface region (Fig. S4C). Radiologist blinded to the experiment protocol measured the signal intensity 4 times for every dog, and then averaged the recorded signal intensity.

2.15. Sample collection and gross observation

After the dogs (n = 13/group) were sacrificed at postoperative month 3, we carefully dissected the humerus, infraspinatus tendon, infraspinatus muscle and acromion, and then photographed for gross observation. The lateral edge of the infraspinatus muscle and the tendon stump were identified to act as markers for the evaluation of repair integrity. If the tendon stump was medial to the repair site or the muscle edge was medial to the acromion as described previously, we determined the repair integrity as gap healing [54]. The gap healing rate was calculated.

2.16. Micro-CT

Five specimens randomly selected from the harvested 13 specimens in each group were fixed with 4% neutral buffered formalin and then remove the residual formalin by running water. After that, the humeral head of specimens with infraspinatus tendon were scanned using a micro-CT (410 Versa, ZEISS, Solms, Germany) with a 20 μm isotropic voxel resolution under 60 kV voltage. After obtaining 3D reconstruction images, we selected a cube ROI (about 10 mm × 10 mm × 10 mm) at the surface of the repaired infraspinatus tendon insertion footprint, which contained the bony footprint and the distal portion of infraspinatus tendon. Three ROIs per animal were randomly selected to measure the bone volume/total volume (BV/TV), trabecular thickness (Tb.Th) and trabecular number (Tb.N), which were then averaged for the following statistical comparison.

2.17. Histological assessment

After micro-CT scanning, the 5 specimens were decalcified with 10% EDTA, embedded in paraffin and sagittally sectioned with 5 μm thickness through the long axis of the infraspinatus tendon. After the sections were stained with H&E, Safranine O/fast green (SO/FG), MT and SR, they were captured using a light or polarized microscope (Eclipse CI, Nikon, Japan). The regenerated infraspinatus tendon insertion was semiquantitatively analyzed by two blinded teammates (C.C and Y.C) with a histological score system adapted from Ide J et al. and Shah SA et al. [55,56] **(Table S5)**, and the proportion of regenerated enthesis tissue at the healing site was also semiquantitatively assessed.

2.18. Biomechanical test

The other 8 specimens in each group were prepared for biomechanical test, and the intact infraspinatus tendon insertions (INT group) harvested from the non-surgical site were also tested as a strength baseline of infraspinatus tendon enthesis for comparison. Biomechanical test was performed on the specimens of the CTL, EG, and INT groups with uniaxial tensile loading (MTS Systems Corp, USA). In brief, after the specimens were thawed overnight at 4 °C, the periarticular connective soft tissues and the suture material were carefully dissected. The humeral shaft of specimen was fixed in a custom-made jig by several screw fasteners, while infraspinatus tendon end was wrapped with a gauze and clamped by an air pressure-controlled clip. The gauze was used to increase the friction between tendon end and clip. After preloading with 1 N, the specimen was pulled to rupture along myotility direction of infraspinatus muscle at a rate of 30 mm/min. Failure load (N) was obtained from the recorded load-displacement curve, and stiffness (N/cm) was calculated from the linear portion of this curve with Office Excel 2020 (Microsoft Corp). During testing, 0.9% saline was dropped into the specimen surface to keep them in a fresh state.

2.19. Statistical analysis

All values were expressed as the mean ± SEM. For the in-vitro experiments, we repeated it at least three times. The unpaired *t*-test was used for the comparison between two groups, while one-way ANOVA with Bonferroni's post hoc test was used for the comparison above two groups. As for the in-vivo experiments, the results were compared using a one-way ANOVA with Bonferroni's post hoc test. Mann-Whitney U *t*-test was used to test for differences in histological scores for the regenerated infraspinatus tendon enthesis. Fisher's exact test was used to test for differences in the gap healing rate. Across the calcified fibrocartilage zone of O-BDEM, regression analyses of the correlation between the Ca or P intensities and sample position were determined. A value of $P < 0.05$ was considered statistically significant. The analyses were performed using the SPSS 25.0 software (SPSS, USA).

3. Results

3.1. Optimizing decellularization approach for fabricating O-BDEM

In this study, we optimize the current acellular protocol for the compact enthesis tissue. Firstly, large-sized NET harvested from a canine infraspinatus tendon enthesis was partly decalcified in a sterile environment, and then this decalcified enthesis tissue specimens were sliced into "book" shape parallel to myotility direction with a thickness of 250 μm, which is the minimum thickness required to retain the tensile properties of NET (Fig. S1). Secondly, the results of DAPI staining and DNA content indicated that BDET should be rinsed in our VAD at least 3 times to completely clear the cellular components (Fig. S2). Thus, 3 times of rinsing in our VAD was selected as the optimized protocol for fabricating O-BDEM (Fig. S2, and movie S1).

Compared with the conventional protocol, our optimized protocol shortened the acellular time from 16 h to 7 h (Fig. S2), and removed the cellular components of enthesis tissue. The sections of C-BDEM or O-BDEM stained with H&E or DAPI showed no extensive cell nuclei (Fig. 2A). Quantitively, the amount of DNA in the NET was about 1069.34 ± 128.73 ng/mg, which was reduced to 34.59 ± 8.20 ng/mg and 33.66 ± 8.67 ng/mg in the C-BDEM or O-BDEM, respectively (Fig. 2C). Additionally, the O-BDEM preserved more collagen and proteoglycans compared to the C-BDEM (Fig. 2A). SR-FTIR analysis together with SR staining indicated that the collagen distribution in both C-BDEM and O-BDEM were similar to that in the NET, but the collagen content lost in the bony and tendinous zones of O-BDEM was only about 10.81% and 29.63%, whereas the collagen content in the bony and tendinous zones of C-BDEM lost about 41.71% and 32.58%. (Fig. 2B). The collagen contents in the fibrocartilaginous zone of NET, C-BDEM, and O-BDEM were similar without any significant difference (Fig. 2A). Further, SR-FTIR analysis combined with TB staining showed that the proteoglycans distribution in the C-BDEM and O-BDEM was partly preserved after decellularization, and the proteoglycans content decreased by about 43.81% and 42.47% in the fibrocartilaginous and tendinous zones of C-BDEM, respectively (Fig. 2B). In O-BDEM, proteoglycans showed only an 18.05% and 39.46% decrease in the fibrocartilaginous and tendinous zones, respectively. The bony zone of NET, C-BDEM, or O-BDEM was almost the same in proteoglycans content.

Using SDS-PAGE (Fig. S5A), we found that the protein bands at low molecular weights almost disappeared in the C-BDEM and O-BDEM, whereas the protein bands at high molecular weights were similar among NET, C-BDEM, and O-BDEM. Further, NET, C-BDEM, or O-BDEM samples were digested with trypsin, and then analyzed by LC-MS/MS combined with a label-free quantification method. The resulting signal distribution from different samples indicated that 1526 protein hits were identified within NET samples compared to 212 hits in C-BDEM and 230 hits in O-BDEM (Fig. 2D). ECM proteins were identified by querying the lists of unique proteins in NET, C-BDEM, or O-BDEM with the UniProt database for the subcellular location search terms "extracellular" combined with the cellular component search terms "extracellular zone" by the Gene Ontology Consortium [43,44]. Following the decellularization process, the number of ECM proteins in C-BDEM decreased from 145 to 65, while, in O-BDEM, the number of ECM proteins decreased from 145 to 72 (Fig. 2D&E). This indicates that the ECM proteins in the C-BDEM or O-BDEM were selectively preserved during decellularization, but O-BDEM preserved better than the C-BDEM in the number of ECM proteins. Additionally, the abundance of main ECM proteins was similar in C-BDEM or O-BDEM (Fig. S5B). All proteins identified by LC-MS/MS are shown in Supplementary Table S6.

After the tensile test, we found the failure load of the C-BDEM and O-BDEM decreased slightly compared with that of NET, but no significant difference was found among them (Fig. 2F). Meanwhile, the stiffness of the O-BDEM showed a litter higher value than that of C-BDEM without significant difference, but both of them were significantly lower than the NET (Fig. 2F).

3.2. Evaluating the gradient mineralization of O-BDEM

Using synchrotron radiation-based micro X-ray fluorescence (SR-μXRF), the distribution of Ca and P at the O-BDEM and NET was mapped clearly (Fig. 3A&B). Fortunately, the mapping images showed that the distribution manner of Ca and P in the O-BDEM was still similar to the NET, as characterized by a shape increase in the calcified fibrocartilage zone from the tendon end to the bony end in an exponential manner (Fig. 3C&D). Regrettably, owing to part decalcification, the Ca content in the bony zone of O-BDEM decreased about 60% compared to the bony zone of the NET with a significant difference. The Ca content in the tendinous zone of the NET and O-BDEM was very low, with no significant difference. P content showed a similar decrease to that of the Ca content (Fig. 3C&D). These results indicate that our protocol could acquire a O-BDEM showing a similar distribution of mineral substance to native enthesis.

3.3. Synthesis of C-BMP-2, C-TGF-β3, C-GDF-7 and their bioactivity evaluation

To avoid the influence of the fused CBP on the active domains of BMP-2, TGF-β3, or GDF-7, a linker sequence was used to link the CBP with the active domain of GF (Fig. 4A). Protein sequences of BMP-2, C-BMP-2, TGF-β3, C-TGF-β3, GDF-7, and C-GDF-7 were listed in Table S1. After BMP-2, C-BMP-2, TGF-β3, C-TGF-β3, GDF-7, and C-GDF-7 were synthesized and purified, they were identified using SDS-PAGE together with western-blotting (Fig. S6A). According to literature, we isolated USCs from healthy human urine (Fig. S7), which also showed multilineage potential with bone marrow mesenchymal stem cells (BMSCs) [37]. In order to comparatively evaluate the bioactivity difference of NAT-GFs or CBP-GFs, the two GFs were respectively added into culture medium of hUSCs (Fig. S6B). Cellular immunofluorescent assay combined with qRT-PCR results showed that BMP-2 and C-BMP-2, TGF-β3 and C-TGF-β3, GDF-7, and C-GDF-7 presented equal inducibility in the osteogenic, chondrogenic, and tenogenic differenti C-BMP-2 solution (8 μM), C-TGF-β3 solution (6 μM), C-GDF-7 solution (8 μM) were respectively immersed into the bone zone, fibrocartilage zone, and tendon zone of O-BDEM with the help of a custom-designed setup, thus zone-specifically tethering CBD-GFs into O-BDEM to fabricate a CBP-GFs/O-BDEM.

ation of hUSCs, respectively. This result determines that the bioactivity of CBP-GFs was not influenced by the fused CBP, indicating the C-BMP-2, C-TGF-β3, and C-GDF-7 can be zone-specifically tethered into the O-BDEM to improve its bioactivities (Fig. 4B).

3.4. Binding ability of C-BMP-2, C-TGF-β3, C-GDF-7 on the collagen of O-BDEM

To evaluate the collagen-binding ability of C-BMP-2, C-TGF-β3, and C-GDF-7, collagen-rich O-BDEM were carefully cut into a DBM, DFM, or DTM, respectively; then, equimolar amounts of BMP-2 or C-BMP-2, TGF-β3 or C-TGF-β3, and GDF-7 or C-GDF-7 were respectively added to the DBM, DFM, and DTM (Fig. 4C). The binding ability of CBP-GFs on the collagen of O-BDEM was determined with a modified ELISA method [50]. As shown in Fig. 4C, at concentrations of 2 μM, 4 μM, 6 μM, 8 μM, 10 μM, and 12 μM, the OD450 of CBP-GFs tethered scaffold presented significantly higher value than that of NAT-GFs tethered scaffold ($P < 0.05$). This result indicated that CBP-GFs showed a stronger binding ability to O-BDEM than NAT-GFs. According to Fig. 4C, the NAT-GFs and CBP-GFs exhibited a dose-dependent binding mode, 8 μM BMP-2, 6 μM TGF-β3, and 8 μM GDF-7 nearly reach the saturation binding amount, thus we used the concentrations for the following *in-vitro* and *in-vivo* study.

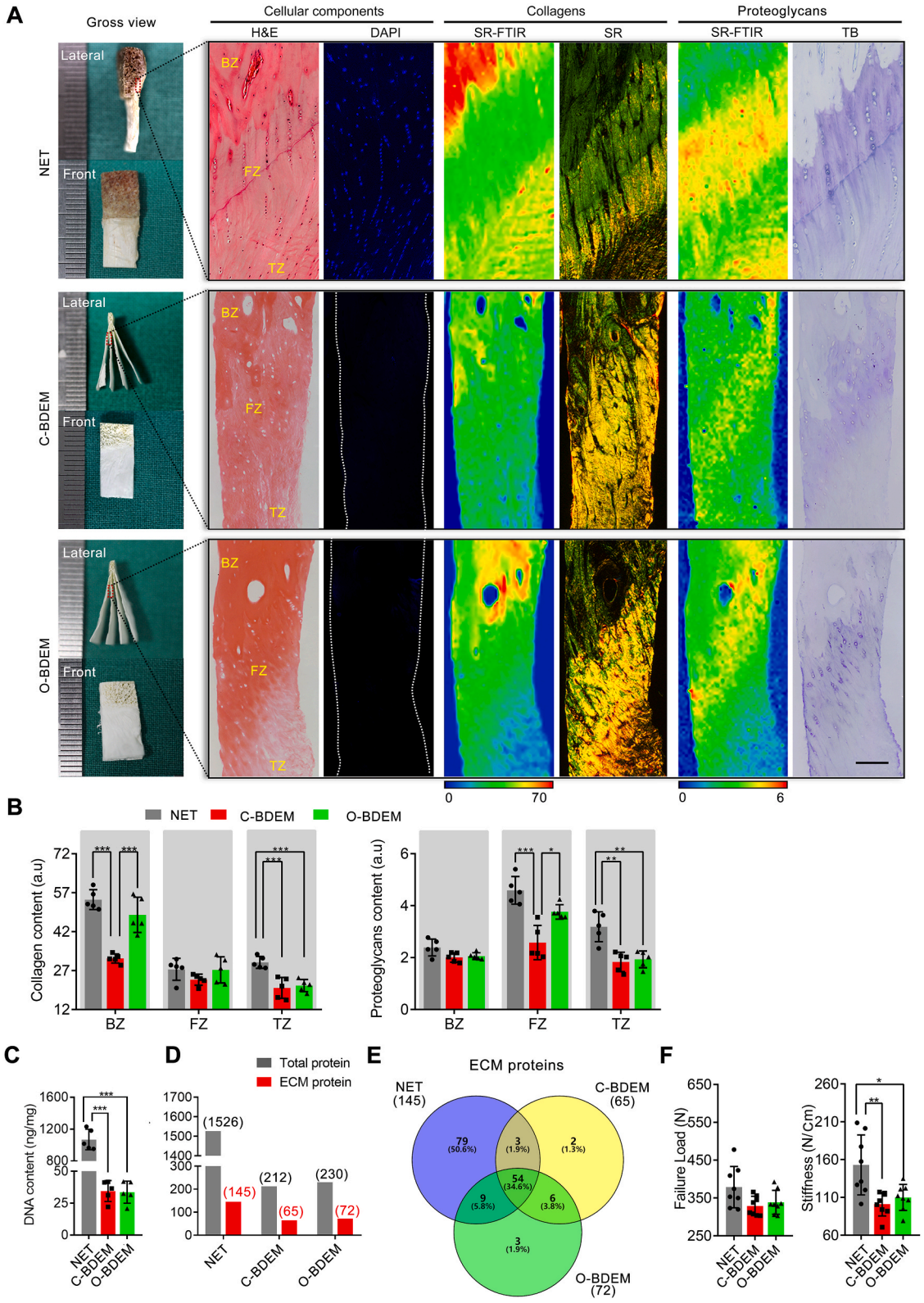

Fig. 2. Characteristic differences between C-BDEM and O-BDEM. (A) Gross features, cellular components, the distribution and content of collagens, the distribution and content of proteoglycans in the NET, C-BDEM, or O-BDEM. H&E and DAPI for observing cellular components. SR-FTIR together Sirius red (SR) staining for evaluating the distribution and content of collagen. SR-FTIR combined with toluidine blue (TB) staining for evaluating the distribution and content of proteoglycans. Bar = 100 μm. (B) Collagen and proteoglycans contents in the bony zone, fibrocartilaginous zone or tendinous zone of the NET, C-BDEM or O-BDEM. (C) DNA content in the NET, C-BDEM, or O-BDEM. (D) Numbers of total proteins and ECM proteins detected in the NET, C-BDEM, or O-BDEM. (E) Venn diagram with the number of ECM proteins identified in the NET, C-BDEM, or O-BDEM. (F) Failure load and stiffness of the NET, C-BDEM, or O-BDEM. BZ: bony zone, FZ: fibrocartilaginous zone, TZ: tendinous zone. All data are presented as the mean ± SEM (n = 5). *$P < 0.05$, **$P < 0.01$, ***$P < 0.001$ (ANOVA with Bonferroni's test).

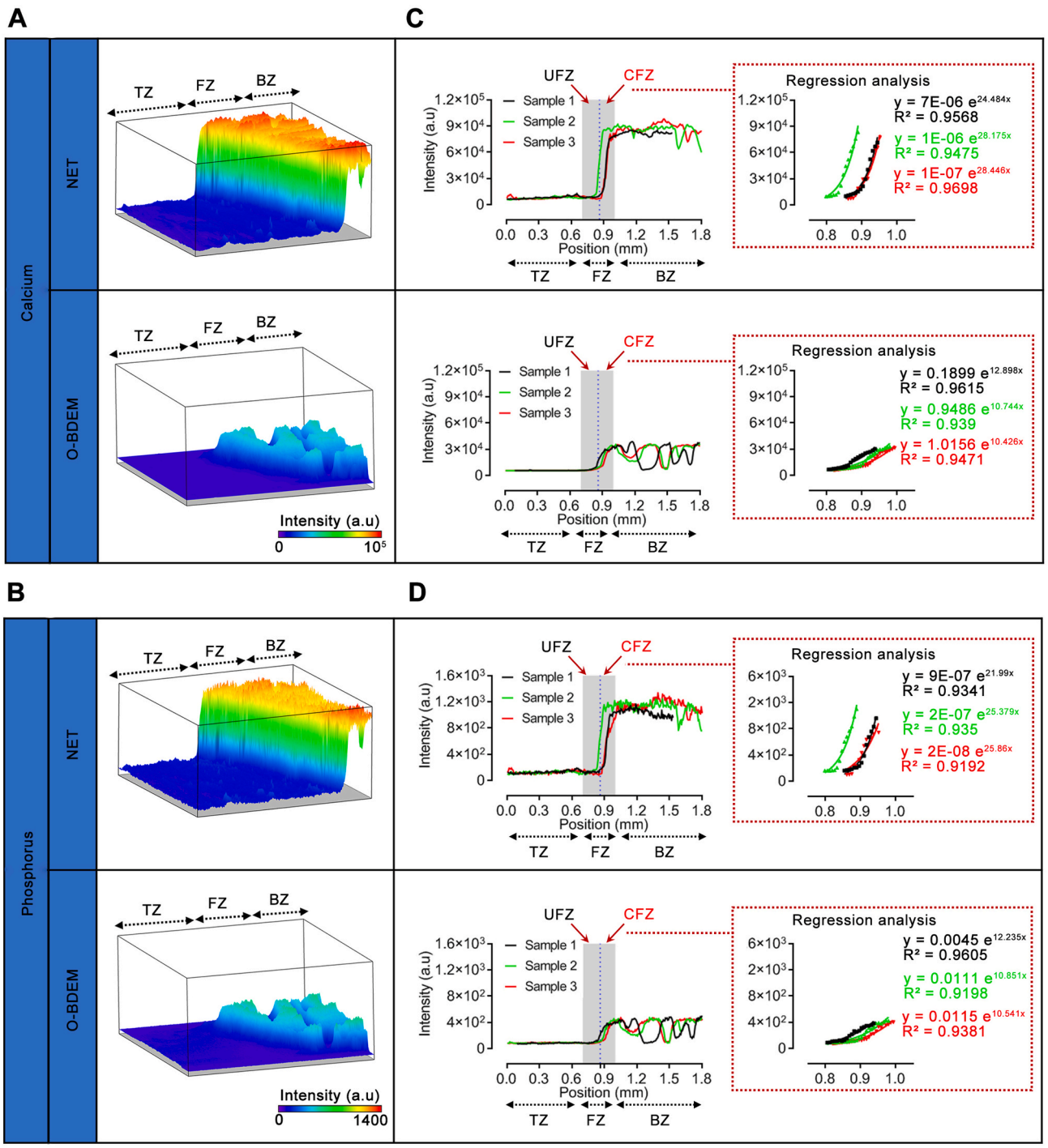

Fig. 3. Mineral distribution in the O-BDEM. (A&B) 3D representations of the calcium (Ca) distribution and phosphorus (P) distribution in a small area (1.806 mm × 0.504 mm) based on the SR X-ray-induced fluorescence intensity from NET and O-BDEM. Their intensity counts are reported by the color-coding scale bar. BZ: bony zone, FZ: fibrocartilaginous zone, TZ: tendinous zone. (C&D) Line scans showed that Ca intensity and P intensity sharply increased from the tendon end to the bony end across the calcified fibrocartilage zone (CFZ), and regression analyses of region-dependent distribution of Ca and P in O-BDEM reveal an exponential fit at this CFZ. The blue dotted line indicates the "tidemark". CFZ: calcified fibrocartilaginous zone, UFZ: uncalcified fibrocartilaginous zone.

3.5. In-vitro release pattern of C-BMP-2, C-TGF-β3, C-GDF-7 from CBP-GFs/O-BDEM

To evaluate the controlled release of GFs from CBP-GFs/O-BDEM *in-vitro*, 8 μM BMP-2 or C-BMP-2, 6 μM TGF-β3 or C-TGF-β3, 8 μM GDF-7 or C-GDF-7 were tethered into the DBM, DFM, or DTM, respectively; after horizontal shaker in PBS, every one day, the residual NAT-GFs or CBP-GFs in scaffold was measured using the above-mentioned modified ELISA method (Fig. 4D). Our results show that the CBP-GFs released from CBP-GFs/O-BDEM obviously slower than the NAT-GFs. After rinsing in PBS for 9-day, only about 3.64 ± 0.71%, 3.90 ± 0.53%, and 4.84 ± 0.49% of BMP-2, TGF-β3, and GDF-7 still remained on the DBM, DFM, and DTM, respectively; whereas C-BMP-2, C-TGF-β3, and C-GDF-7 remained about 34.54 ± 2.23%, 37.98 ± 2.54%, and 35.17 ± 2.08% on the DBM, DFM, and DTM, respectively (Fig. 4D).

To further confirm the controlled release of GFs from CBP-GFs/O-

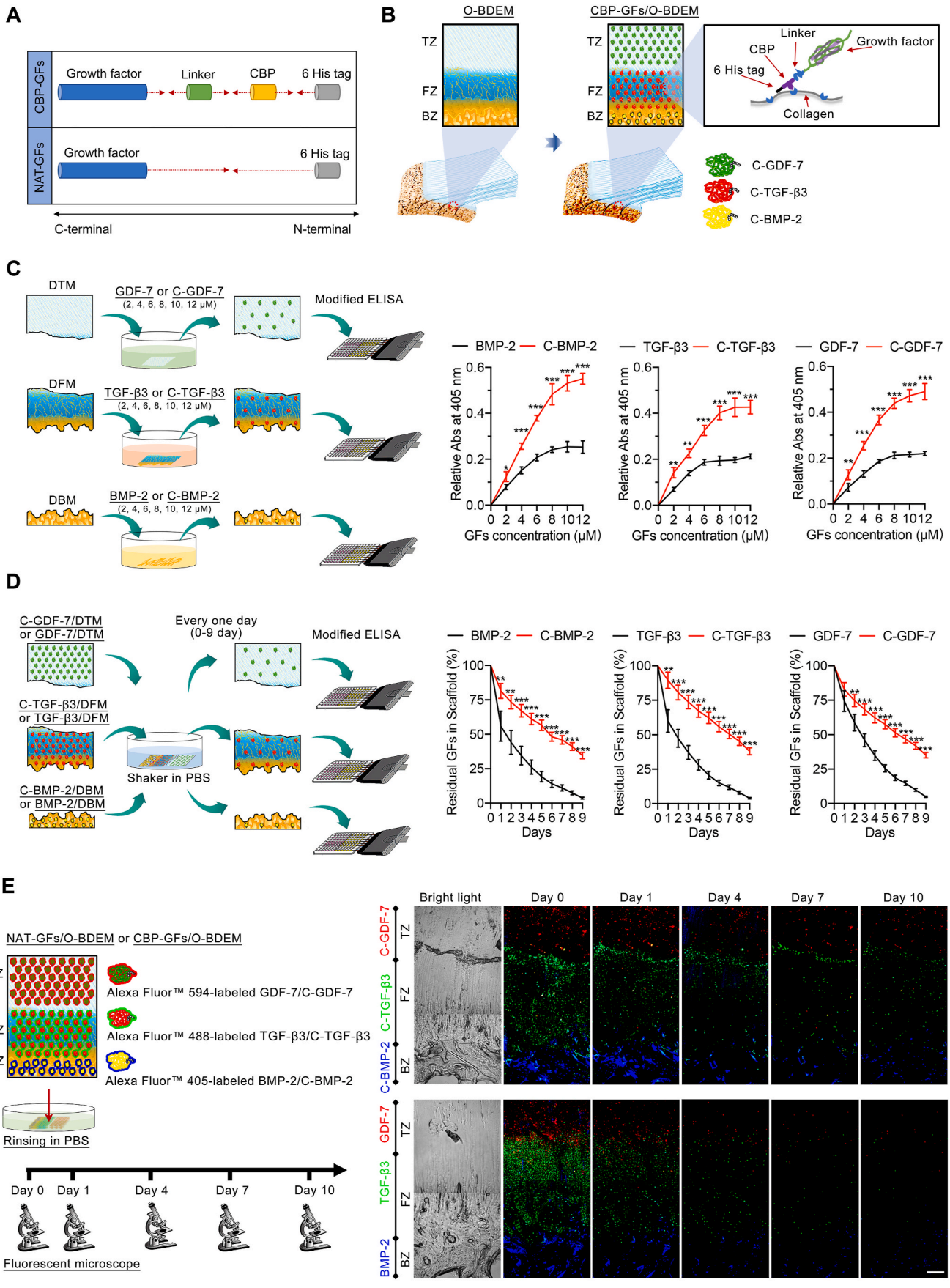

(caption on next page)

Fig. 4. The binding ability of C-BMP-2, C-TGF-β3, C-GDF-7 on the collagen of O-BDEM, and *in-vitro* release pattern of C-BMP-2, C-TGF-β3, C-GDF-7 from CBP-GFs/O-BDEM. (A) Schematic illustration of the chemical structure of the CBP-GFs, a collagen-binding peptide (CBP) was fused into the N-terminus of an active fragment of GFs using a linker sequence. (B) Schematic illustration of the preparation of CBP-GFs/O-BDEM. C-BMP-2, C-TGF-β3, C-GDF-7 were region-specifically tethered on the BZ, FZ, and TZ of O-BDEM by a collagen-binding peptide (CBP), thus constructing a CBP-GFs/O-BDEM. BZ: bony zone, FZ: fibrocartilaginous zone, TZ: tendinous zone. (C) The binding curves of BMP-2 or C-BMP-2, TGF-β3 or C-TGF-β3, GDF-7 or C-GDF-7 on the collagens of DBM, DFM, DTM. (D) The curves showed the residual proportions of BMP-2 or C-BMP-2, TGF-β3 or C-TGF-β3, GDF-7 or C-GDF-7 in the DBM, DFM, DTM after rinsing in PBS every one day. (E) The residual NAT-GFs or CBP-GFs in the BZ, FZ, and TZ of O-BDEM after rinsing in PBS for 1 day, 4 days, 7 days, 10 days. BMP-2 and C-BMP-2, TGF-β3 and C-TGF-β3, GDF-7 and C-GDF-7 were labeled with Alexa Fluor™ 405, Alexa Fluor™ 488, Alexa Fluor™ 594, respectively. Bar = 200 μm. All data are presented as the mean ± SEM (n = 4). $^{*}P < 0.05$, $^{**}P < 0.01$, $^{***}P < 0.001$ (independent samples *t*-test).

BDEM *in-vitro*, we labeled the NAT-GFs and CBP-GFs with different fluorescent dyes, the three labeled NAT-GFs or the three labeled CBP-GFs were zone-specifically tethered into the bony zone, fibrocartilaginous zone, tendinous zone of O-BDEM; after horizontal shaker in PBS, every three days, the residual labeled NAT-GFs or labeled CBP-GFs in scaffold were observed under a fluorescent microscope (Fig. 4E). The fluorescent images showed that C-BMP-2, C-TGF-β3, and C-GDF-7 could zone-specifically tether to the bony zone, fibrocartilaginous zone, tendinous zone of O-BDEM as well as release from it in a sustained manner (Fig. 4E). These results indicated that CBP-GFs/O-BDEM was suitable as a controlled delivery system for the zone-specific release of BMP-2, TGF-β3, and GDF-7.

3.6. CBP-GFs/O-BDEM shows zone-specific inducibility on stem cell differentiation in-vitro

O-BDEM were carefully cut into an DBM, DFM, and DTM, then 8 μM BMP-2 or C-BMP-2, 6 μM TGF-β3 or C-TGF-β3, 8 μM GDF-7 or C-GDF-7 were respectively tethered into the DBM, DFM, or DTM to acquire BMP-2/DBM, C-BMP-2/DBM, TGF-β3/DFM, C-TGF-β3/DFM, GDF-7/DTM, C-GDF-7/DTM. After that, the DBM, DFM, and DTM were placed together closely in a culture dish, the BMP-2/DBM, TGF-β3/DFM, and GDF-7/DTM were also placed together closely in another culture dish, the C-BMP-2/DBM, C-TGF-β3/DFM, and C-GDF-7/DTM were also placed together closely in another culture dish (Fig. 5A). After seeding hUSCs on these scaffolds, the expression of osteogenic (Runx2, Ocn), chondrogenic (Sox9, Acan), tenogenic (Scx, Tnmd) specific genes in hUSCs were evaluated by qRT-PCR (Fig. 5A). On day 5 after seeding, hUSCs on the C-BMP-2/DBM showed significantly higher expression of osteogenic-specific genes compared to the hUSCs on the other scaffold or the TCPS (as control). Moreover, the C-TGF-β3/DFM significantly enhanced the expression of chondrogenic-specific genes in the hUSCs compared with the other scaffold or the TCPs. We also found that the tendon-specific genes expressed highest in the C-GDF-7/DTM among all scaffold. These results were further assessed by cellular immunofluorescent assay. The immunofluorescent images (Fig. 5B) showed that the Runx2 protein expressed highest in the C-BMP-2/DBM, suggesting the preferential differentiation of hUSCs into the osteogenic lineage in this zone. Meanwhile, the hUSCs on the C-TGF-β3/DFM expressed the highest Sox9 protein, indicating their preferential differentiation into the chondrogenic lineage in this zone. Similarly, the highest expression of Scx protein was located in the C-GDF-7/DTM, implying the preferential differentiation of hUSCs into the tenogenic lineage. These results indicate that CBP-GFs/O-BDEM can realize zone-specific and controlled release of stem cell differentiation stimulators, thus spatially inducing the interacted stem cells toward osteogenic, chondrogenic, and tenogenic lineages *in-vitro* (Fig. 5C).

3.7. CyTOF reveals the in-vivo immunological response of CBP-GFs/O-BDEM at single-cell resolution

CyTOF, the latest technique in flow cytometry, was applied for analyzing the murine blood for characterizing the CBP-GFs/O-BDEM or AHDM-induced immune responses in a supraspinatus tendon repair model, and systematically deciphered the interactions between the host and implants. AHDM has been used in the clinic for repairing wounds and large RC tears [57,58]; thus, it was included as a reference for evaluating the immunological response of the implanted CBP-GFs/O-BDEM. At day 21 post-implantation, blood samples were pumped from the mouse heart in the CTL (without implantation), CBP-GFs/O-BDEM and AHDM groups, barcoded with unique metal isotopes before staining with the antibody panel (**Table S4**), and then evaluated with CyTOF to extensively define immune cell populations as follows: neutrophils ($CD45^+CD11b^+Ly6g^+$), macrophages ($CD45^+CD11b^+F4/80^+$), monocytes ($CD45^+CD11b^+Ly6c^+$), dendritic cells (DC cells) ($CD45^+CD11b^+CD11c^+$), natural killer (NK) cells ($CD45^+CD11b^+CD49b^+$), $CD4^+$ T cells ($CD45^+CD3^+CD4^+$), $CD8^+$ T cells ($CD45^+CD3^+CD8^+$), γδT cells ($CD45^+CD3^+TCR\gamma\delta^+$), and B cells ($CD45^+B220^+$). After identifying the nine immune cell populations based on marker-expression similarity, we used SPADE (spanning-tree progression analysis of density-normalized events) algorithm to construct a minimum spanning tree of hierarchically-related nodes in which the node size represents the number of cells within each population, thus comparatively evaluating the abundance of those cell populations among the three groups (Fig. 6A) [59]. The live single cells were sorted out using cisplatin as a marker (Fig. S8), meanwhile all innate and adaptive immune cells were identified using CD45. Innate immune cells (neutrophils, macrophages, monocytes, DCs, and NK cells), are involved in the foreign-body reaction by clearing damaged cells and recruiting immune effector cells [60]. Herein, the neutrophils (Fig. 6B), macrophages (Fig. 6B), monocytes (Fig. S9), DC cells (Fig. S9), and NK cells (Fig. S9) of blood samples were manually gated, showing that the CBP-GFs/O-BDEM group contained a much lower proportion of neutrophils, macrophages, and monocytes when compared to the CTL and AHDM group (Fig. S9). The proportion of DCs in the CBP-GFs/O-BDEM group showed a similar frequency to the CTL group, but both of them were lower than the AHDM group. Furthermore, the NK cells in both the CBP-GFs/O-BDEM group and AHDM group showed higher proportion than that in the CTL group; however, the proportion in the AHDM group was higher than that in the CBP-GFs/O-BDEM group.

Besides, adaptive immune cells also play a critical role in the immunological reaction to implantation, which participate in anti-foreign reaction by inducing lymphocytes mainly comprising B and T cells. Herein, the B cells (Fig. 6C), $CD8^+$ T cells (Fig. S10), $CD4^+$ T cells (Fig. S10), and γδ T cells (Fig. S10) in blood samples were manually gated. From our results (Fig. 6C), the proportion of B cells and all T cells in the CBP-GFs/O-BDEM group were higher than those in the AHDM group. As for $CD8^+$ T cells, their proportions were also higher in the CBP-GFs/O-BDEM group. The $CD4^+$ T cells and γδ T cells in both CBP-GFs/O-BDEM group and AHDM group showed slightly higher proportion when compared to that in the CTL group, while no obvious differences were found between them. Collectively, these results indicated that the CBP-GFs/O-BDEM was low immunogenicity similar to the AHDM that has been approved for augmenting the injured RC in the clinic [57].

3.8. Local immunological response induced by the implanted CBP-GFs/O-BDEM

Local immunological response induced by the CBP-GFs/O-BDEM or AHDM was also evaluated (Fig. S11). **T**he regenerated RC enthesis in the CTL and CBP-GFs/O-BDEM groups presented a similar gross appearance to the native RC enthesis, while more blood vessels were formed at the

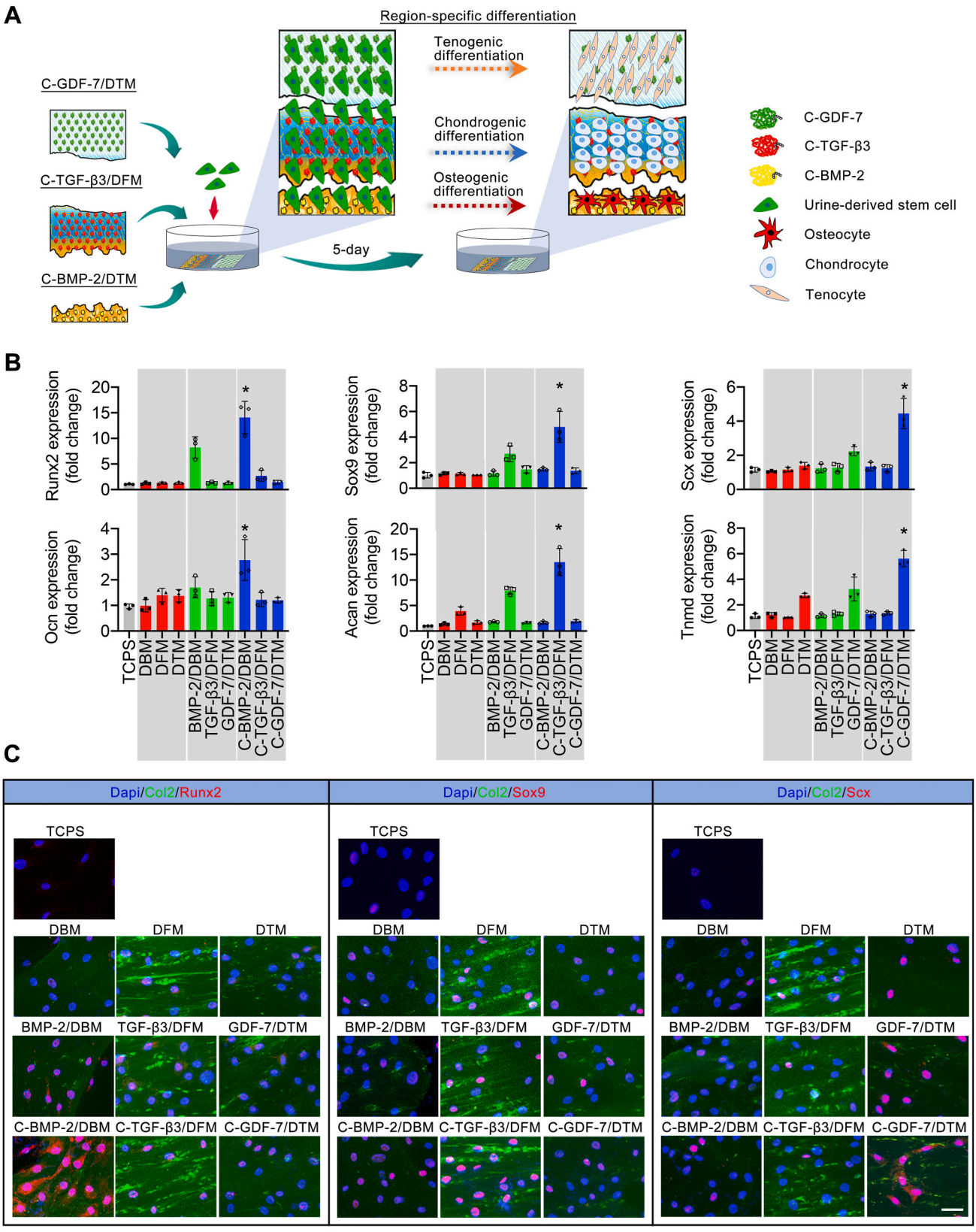

Fig. 5. CBP-GFs/O-BDEM zone-specifically induce the interacted hUSCs toward osteogenic, chondrogenic, and tenogenic lineages. (A) Schematic representations of the osteogenic, chondrogenic, or tenogenic differentiations of hUSCs under the zone-specific stimulations of C-BMP-2/DBM, C-TGF-β3/DFM, C-GDF-7/DTM. (B) the qRT-PCR results show that the osteogenic genes (Runx2, Ocn), chondrogenic genes (Sox9, Acan), and tenogenic genes (Scx, Tnmd) expressed in hUSCs co-cultured on the TCPS or the C-BMP-2/DBM, C-TGF-β3/DFM, C-GDF-7/DTM, BMP-2/DBM, TGF-β3/DFM, GDF-7/DTM, DBM, DFM, DTM for 5-days. $^{*}P < 0.05$ compared to the TCPS or the other scaffolds. (C) Immunofluorescent assay showed the osteogenic (Runx2), chondrogenic (Sox9), and tendon (Scx) markers expressed in hUSCs cultured on TCPS or the C-BMP-2/DBM, C-TGF-β3/DFM, C-GDF-7/DTM, BMP-2/DBM, TGF-β3/DFM, GDF-7/DTM, DBM, DFM, DTM for 5-days. Bar = 50 μm. All data are presented as the mean ± SEM (n = 3). $^{*}P < 0.05$ (independent samples *t*-test).

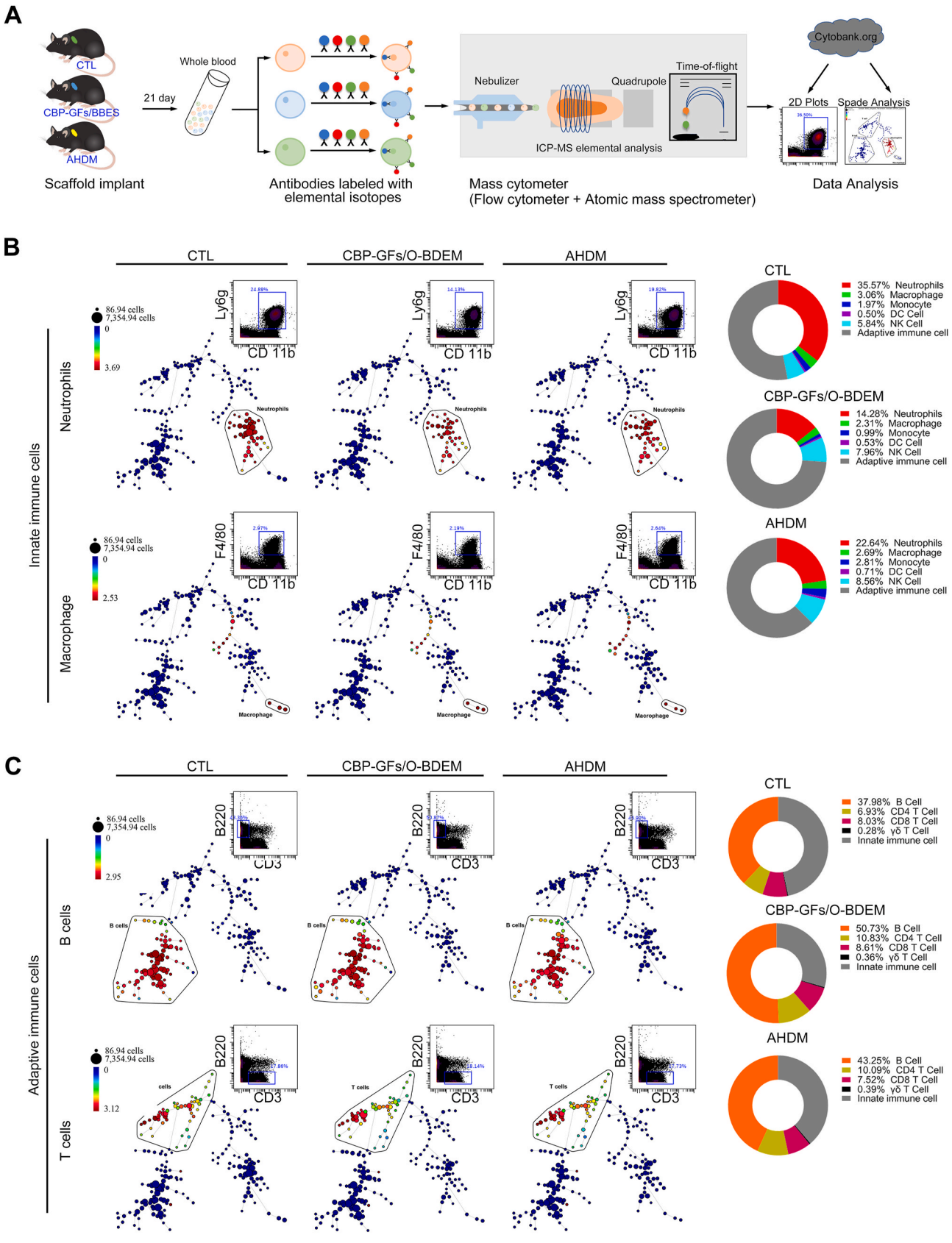

(caption on next page)

Fig. 6. Differential abundances of systematic innated and adaptive immune cell populations in the mice blood samples from CTL, CBP-GFs/O-BDEM and AHDM groups. (A) Schematic diagram of the experimental procedure. Mice blood samples from CTL, CBP-GFs/O-BDEM and AHDM groups were collected respectively at postoperative 21-day. After lysis of the red blood cells, these pooled cells were stained with antibodies conjugated to elemental isotopes, and then analyzed using a CyTOF machine. The immune cell populations were manually gated, and then identified using SPADE algorithms. (B) The SPADE tree and dot plots analysis shows the abundance of $CD11b^{+}Ly6g^{+}$ neutrophils or $F4/80^{+}$ macrophage in each group. In the SPADE diagram, the number of immune cell populations were represented with node size, and the colored gradient of the node correlates with the median intensity of marker-expression. The relative abundance of innate immune cells (monocytes, macrophages, neutrophils, DC cells and NK cells) among three groups, as calculated from the SPADE analysis. (C) The SPADE tree and dot plots analysis shows the frequency of B and T cells in CTL, CBP-GFs/O-BDEM and AHDM groups. The relative abundance of adaptive immune cells (B cells, $CD4^{+}$T cells, $CD8^{+}$T cells, and γδT cells) among three group calculated from the SPADE analysis. All data are presented as the mean ± SEM (n = 3).

subdeltoid fascia in the CBP-GFs/O-BDEM group (Fig. S11B). In the AHDM group, there are some residual AHDM located at the implant site (Fig. S11C). In the H&E-stained sections, fibrotic capsule was formed around the implants obviously in the AHDM group, whereas only a few implants showed such capsules in the CBP-GFs/O-BDEM group (Fig. S11D). Considering that neutrophils and macrophages are the predominant contributors to forming fibrotic capsule [52], we examined the infiltration of neutrophils (Ly6g) and macrophages (F4/80) at the site of implantation using immunofluorescence assay (Fig. S11E). Our results indicate that the fibrotic capsule around the AHDM accumulated more neutrophils and macrophages compared to that around the CBP-GFs/O-BDEM. The accumulation of neutrophils and macrophages at the implant site may limit its integration with the surrounding native tissues. These results indicated that the CBP-GFs/O-BDEM showed the low ability to induce a local immune reaction compared with the AHDM that has been approved for augmenting the injured RC in the clinic [57].

3.9. Constructing enthesis-like graft and its morphology evaluation

After the isolated cUSCs were identified (Fig. S12A), they were cultured to form a cUSC-sheet. Our result showed their trilineage differentiation potential was well preserved, indicating that the cUSCs in cell-sheet form still have good differentiation capabilities (Fig. S12B). After that, three slices of cUSC-sheet were separately interleaved into the page gaps of the CBP-GFs/O-BDEM, and then the other two slices of cUSCs-sheet were used to cover the top and bottom surfaces of the CBP-GFs/O-BDEM for bioengineering an enthesis-like graft (Fig. 7A) (Movie S2). Histologically, five cUSC-sheets containing a large number of cUSCs were layer-by-layer interleaved into the page gaps of CBP-GFs/O-BDEM (Fig. 7B).

3.10. Bioengineering an enthesis-like graft for RC enthesis regeneration in a canine model

After that, the performance of this enthesis-like graft on RC enthesis regeneration was in-vivo evaluated in a canine infraspinatus tendon repair model (Fig. 7C). Enthesis-like graft (EG group) and direct suture (CTL group) were chosen for in-vivo evaluation, while native infraspinatus tendon enthesis was used as intact control (INT group). In view that CBP-GFs/O-BDEM shows the best zone-specific inducibility on the interacted stem cell differentiation *in-vitro*, we did not use the O-BDEM and GFs/O-BDEM to bioengineer the other graft in this study. This is more compliant with ethical requirements for laboratory animals.

At 4, 8, and 12 weeks after implantation, dogs (n = 5/group) were anesthetized with 3% pentobarbital sodium (0.2 ml/kg), and then received clinical MRI examination (Ingenia 3.0T MR system; Philips, Germany) for imaging the regenerated IT enthesis (Fig. S4). At week 4, MRI images from CTL and EG groups showed obvious swelling in the surrounding soft tissue and bone marrow edema in the humeral head when compared with the INT group (Fig. 7D). Meanwhile, the CTL group showed higher signal intensity in the infraspinatus tendon enthesis area compared with the EG group, suggesting heavier edema. At week 8, bone marrow edema in the humeral head of CTL and EG groups displayed a decreasing tendency, indicating the promoted progress in healing process. The surrounding soft tissue shows no obvious hyperintense sign, indicating the swelling regression. Hyperintensity in the infraspinatus tendon enthesis area could be observed in each group, but when compared to 4 weeks, it presented more homogeneous distribution. Besides, the signal intensity of the regenerated infraspinatus tendon enthesis in the CTL group was still significantly larger than that of the EG group, which implies that the infraspinatus tendon enthesis in the EG group regenerated better than the CTL group (Fig. 7D). At week 12, bone marrow edema on the humeral head and swelling on the surrounding soft tissue had almost disappeared. The intensity of the regenerated infraspinatus tendon enthesis in the CTL group remains larger than that of the EG group (Fig. 7D).

At 12 weeks after euthanasia, well-integrated connective tissue was formed spanning the infraspinatus muscle to the humerus in all specimens without evidence for infection or osteoarthritis. In the EG group, the bony zone or tendon segment of the implanted enthesis-like graft integrated well with the greater tubercle of humerus and the ruptured infraspinatus tendon, respectively; The infraspinatus tendon entheses showed a delineated footprint similar to the intact infraspinatus tendon entheses, while the entheses in the CTL group displayed poorly organized fibrous tissue. The tendon stump and the lateral edge of the infraspinatus muscle was used as evaluation criteria for repair integrity. If the tendon stump was medial to the repair site or the muscle edge was medial to the acromion as described previously, we determined the repair integrity as gap healing [54]. The gap healing rate in the EG group was 38.46%, which was lower than the CTL group (46.15%) without significant differences ($P > 0.05$) (Fig. 7E).

At 12 weeks, micro-CT images (n = 5/group) showed that the newly-formed bone at the healing site of the EG group remodeled more mature than that of the CTL group, as characterized by an obvious improvement in bone volume/total volume (BV/TV), trabecular thickness (Tb.Th) and trabecular number (Tb.N) (Fig. 7F). No sign of ectopic bone formation showed in the infraspinatus tendon healing site in both CTL and EG group. Histologically, newly-formed bone at the footprint of IT and structurally integrated well with the ruptured infraspinatus tendon by a fibrous or/and fibrocartilaginous tissue in all groups (Fig. 8A). According to blinded evaluations, 68.40% of the regenerated tissue in the TE group is histologically similar to the native enthesis of the INT group, which comprised of well-orientated fibrous connective tissue (tendon), fibrocartilaginous tissue, and subchondral bone (mix of lamella and woven bones) (Fig. 8B). While, in the CTL group, only 48.47% of the healing site regenerated tissue with similarity to enthesis, and the remaining regenerated tissue was typically comprised of two zones: disorganized fibrous connective tissue with Sharpey fibers and subchondral bone (Fig. 8B). Using a histological score system (Table S5), the EG group showed significantly better histological scores when compared to the CTL group ($P < 0.05$) (Fig. 8C&D). Additionally, no signs of infection, rejection, or untoward immune reactions was showed at the healing site according to histologic assessments.

3.11. The regenerated enthesis recovered biomechanical properties

At postoperative week 12, the specimens (n = 8/group) in the CTL or EG groups recovered about 53.67% and 77.42% of the failure load (N) compared with the INT group, and the EG group presented significantly larger value in failure load than the CTL group ($P = 0.0002$) (Fig. 8E). Meanwhile, the stiffness (N/mm) in the EG group restored significantly better than that of the CTL group ($P = 0.0399$) (Fig. 8E). During

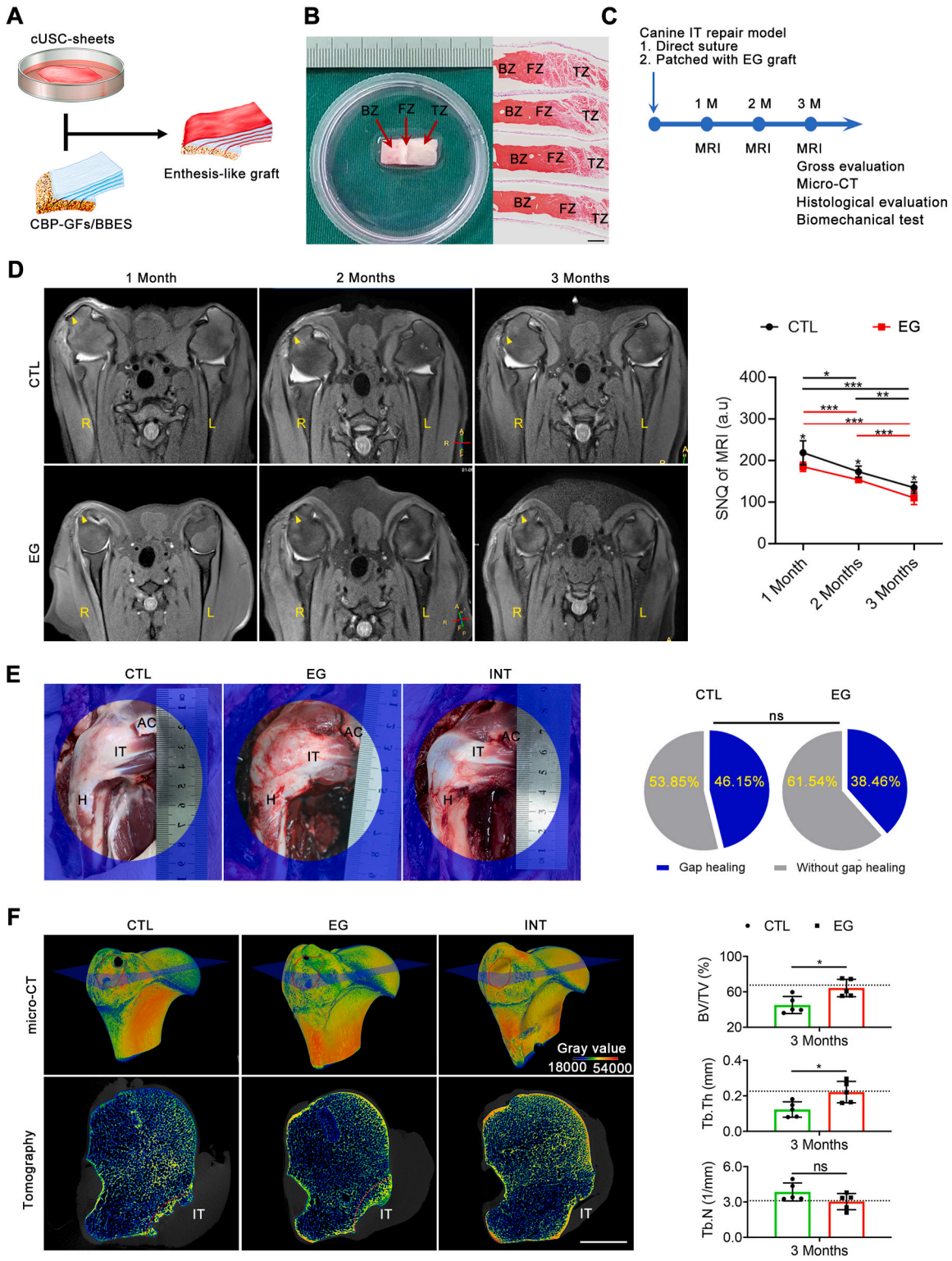

Fig. 7. In-vivo performance of enthesis-like graft on regenerating canine RC enthesis evaluated with MRI, gross observation, micro-CT. (A) Schematic illustration for the construction of enthesis-like graft. (B) Microscopic morphology and H&E-stained imaging of enthesis-like graft. BZ: bony zone, FZ: fibrocartilaginous zone, TZ: tendinous zone. Bar = 250 μm. (C) Flowchart depicting the groups and time points for outcome assessments. (D) Representative MRI scans of the CTL and EG group at postoperative month 1, 2, or 3. The average signal-to-noise quotient (SNQ) of the CTL and EG groups at 1, 2 and 3 months. No difference was found at 2 and 3 months, but at 1 month, the average SNQ of the CTL group was significantly higher than that of the EG group. The injured IT enthesis is marked by a yellow triangle. All data are presented as the mean ± SEM (n = 5). *$P < 0.05$, **$P < 0.01$, ***$P < 0.001$ (Two-way ANOVA with Bonferroni's test). (E) Gross appearances of the regenerated infraspinatus tendon enthesis in a canine model at 3 months (n = 13). AC: acromion, IT: infraspinatus tendon, H: humerus. ns $P > 0.05$ (Fisher's exact test for comparing gap healing rate between CTL and EG groups). (F) Representative micro-CT images of the proximal humerus in the CTL EG or INT group at postoperative month 3. Comparison of the BV/TV, Tb·Th, and Tb·N in newly formed bone among the 3 groups. Red dotted circle shows the IT insertion footprint. Blue quadrangle shows the section position of tomography. Red dotted line indicates the osteotomy site. Bar = 1 cm. All data are presented as the mean ± SEM (n = 5). ns $P > 0.05$, *$P < 0.05$, **$P < 0.01$ (Unpaired *t*-test).

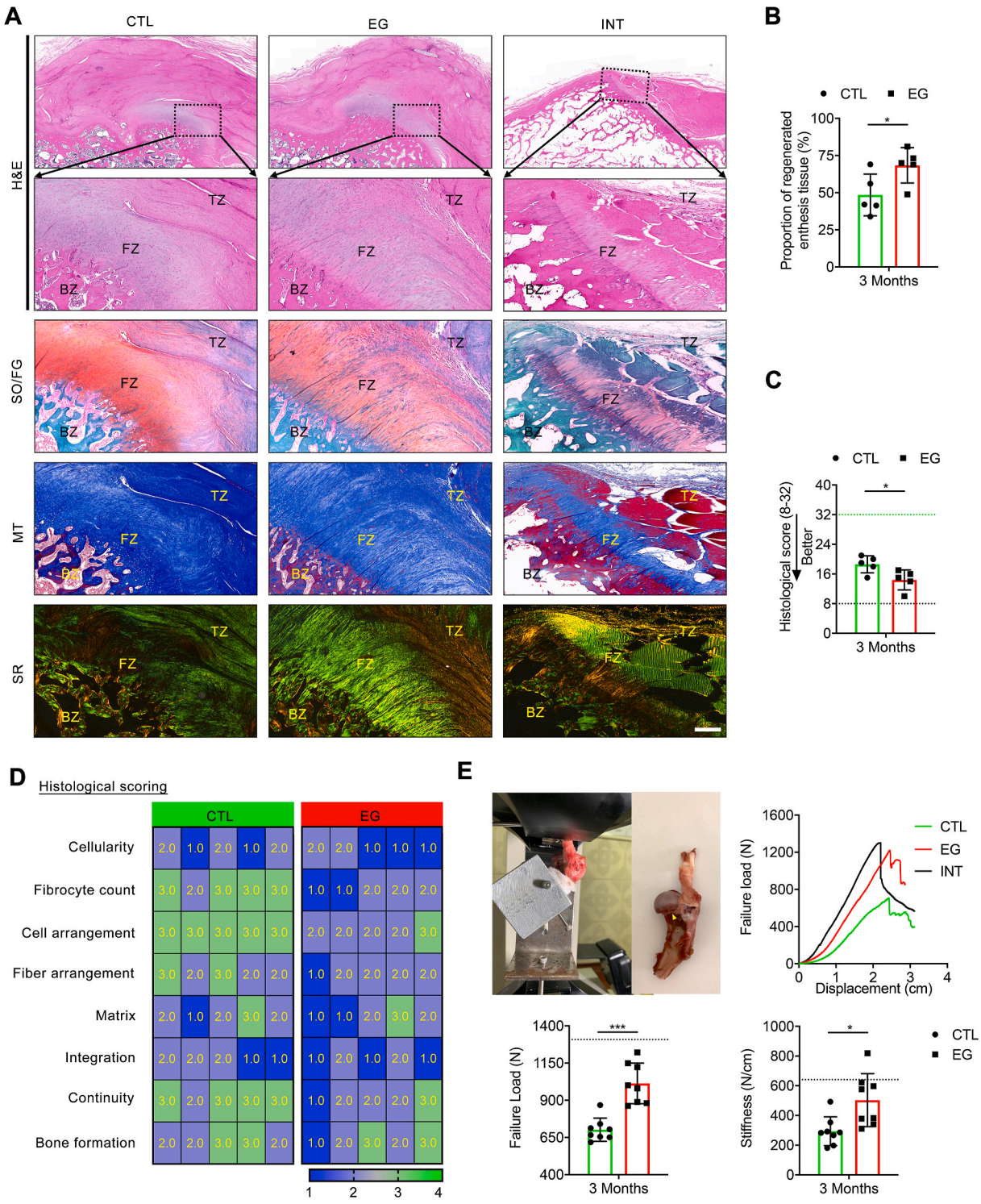

Fig. 8. In-vivo performance of enthesis-like graft on regenerating canine RC enthesis evaluated with histological analyses and mechanical test. (A) Histological analyses of the regenerated enthesis in a canine model. Regenerated infraspinatus tendon enthesis stained with H&E, SO/FG, MT and SR at month 3. Healthy dog was used as an intact control (INT). BZ: bony zone, FZ: fibrocartilaginous zone, TZ: tendinous zone, H&E: hematoxylin and eosin, SO/FG: safranine O/fast green, MT: masson's trichrome, SR: sirius red. Bar = 400 μm. (B) Proportion of regenerated enthesis tissue at the healing site. (C) Histological scores for the regenerated infraspinatus tendon enthesis. Black and green dotted lines, respectively, indicate the perfect score (32 points) and worst score (8 points) in the histological scoring system. $^{*}P < 0.05$, $^{**}P < 0.01$ (Mann-Whitney U *t*-test). (D) Heat map of variables of the histological scoring. (E) Biomechanical test of the regenerated infraspinatus tendon enthesis using a custom-made jig, representative load-displacement curves, failure load and stiffness of the specimens in the CTL, EG and INT groups. The raptured site is marked by a yellow triangle. All data are presented as the mean ± SEM (n = 8). $^{*}P < 0.05$, $^{***}P < 0.001$ (Unpaired *t*-test).

mechanical test, the specimens in both INT group and CTL group ruptured at the IT insertion site, while 6 of 8 specimens from EG groups failed at the insertion site and 2 failed at the tendon mid-substance. The EG group (25.0%) seems to have a higher tendency in mid-substance tear compared to the CTL group (0.0%). However, there are no significant difference between the CTL group and EG group by Fisher's exact test ($P = 0.467$).

4. Discussion

Rapid and functional enthesis regeneration remains a bottleneck during RC repair, and the available enthesis-like grafts for patching RC tear are insufficient, because they were engineered by a scaffold that did not highly mimic native enthesis in morphology, composition, and tensile property, at the same time cannot release stem cell differentiation inducers in a zone-specific manner. In this study, we successfully fabricated a novel scaffold (CBP-GFs/O-BDEM) avoiding the two insufficiencies. CyTOF was novelty applied to determine the low immunogenicity CBP-GFs/O-BDEM at single-cell resolution in a mouse model. Then, we isolated autogenous cUSCs from canine urine and cultured to form cUSC-sheets, which were then sandwiched by the CBP-GFs/O-BDEM to construct a novel enthesis-like graft. The in-vivo function of this enthesis-like graft on RC enthesis regeneration was elucidated using a canine model (Fig. 9). This study provides a new bioengineering strategy for RC repair that may be translated into human patients in the future.

Enthesis tissue exhibits anisotropic structural properties, which gradually vary from tendon tissue to bony tissue. Various conventional isotropic scaffolds have been developed to regenerate the injured enthesis, but these scaffolds just patched the damaged tendon tissue that was not integrated into bones, often resulting in graft failures [61]. Thus, the next generation of scaffold should be designed with a triphasic or even gradient pattern able to mimic the triphasic tissue zone and the mechanical, structural, and compositional graded properties present in the native enthesis. Currently, different research groups have investigated the possibility to fabricate triphasic even gradient scaffolds for enthesis regeneration, such as a bone-ligament attachment using polyethylene glycol diacrylate hydrogel (PEGDA) incorporated with HA [62], a multiphasic poly(ε-caprolactone) (PCL)-PCL/tricalcium phosphate (TCP)-PCL/TCP porous scaffold [63], a stratified scaffold attached through a continuous polyethylene glycol (PEG) hydrogel interface [64]. However, these multi-phased scaffolds only mimic the triphasic or gradient structure at the macro-scale. The design of a multi-phased scaffold able to mimic the micro-scale gradients and components present at the enthesis remains a challenge. Decellularization techniques, as an available protocol to acquire a highly biomimetic scaffold, have been widely used to prepare decellularized extracellular matrix for bone, cartilage, muscle, and tendon regeneration [65,66]. It may be a promising way to fabricate this required scaffold. Histologically, the RC enthesis is a composite tissue including pure dense tendon, uncalcified and calcified fibrocartilage, and bone [5]. The previously developed protocols for bone, cartilage, and tendon decellularization cannot be combined to prepare this composite tissue. Besides, the chondrocytes usually are deeply embedded in a dense and low-porous extracellular matrix [6,17], allowing for limited acellular solution infiltration, which are difficult to absolutely remove the cellular components from large-size enthesis while mostly conserving native extracellular matrix [36,67]. The existing protocols for decellularizing enthesis rely heavily on detergents, such as Triton-X 100 and SDS, and focused on clearing the cell components of tissue, seldom on preserving the structures, components, and tensile resistance [67–72]. Considering that the use of detergents may denature enthesis extracellular matrix proteins even alter its mechanical properties, Liu Q et al. developed an acellular protocol for enthesis decellularization without using detergent [41]; however, this protocol was time-inefficient, and did not consider the preservation of tensile resistance. Moreover, this protocol is designed for decellularizing enthesis tissue from patellar tendon-tibial tuberosity interface, nor for the enthesis tissue from RC insertion. Herein, we proposed an optimal decellularization approach for enthesis tissue from RC insertion, and considered the above-mentioned requirements. With the help of VAD, our decellularization approach significantly shortened the time of decellularization from 16 h into 7 h, preserved more enthesis extracellular matrix (especially the minor matrix components), and well protected the tensile property.

Satisfactory scaffolds for engineering enthesis-like graft should not only have excellent biomimetic properties, but also harbor superior bioactivity in zone-specifically inducing stem cells toward osteogenic, chondrogenic, and tenogenic lineages, thus simultaneously and efficiently inducing triphasic bone-fibrocartilage-tendon structure formation. Several studies indicate that scaffold bioactivities mainly depend on their biomolecules, surface topography, and substrate stiffness, which work together to regulate cell adhesion, matrix production, cell proliferation and/or differentiation during tissue regeneration [73,74–76]. As the inherent biomolecules and structural characteristics of O-BDEM are permanent and unchangeable, the addition of exogenous GFs may be a possible method to improve its bioactivity [13]. Given the triphasic nature of enthesis, multiple GFs should ideally be immobilized zone-specifically into the scaffold to provide the interacted cells with different differentiation stimuli. Thus, in an optimal approach, these GFs should be gradually released from the O-BDEM in a zone-specifical manner. Published literatures have indicated that BMP-2, TGF-β3, and GDF-7 respectively showed superior performance in inducing stem cells toward osteogenic, chondrogenic, and tenogenic lineages [13,23–25], implying that BMP-2, TGF-β3, and GDF-7 are suitable for improving the

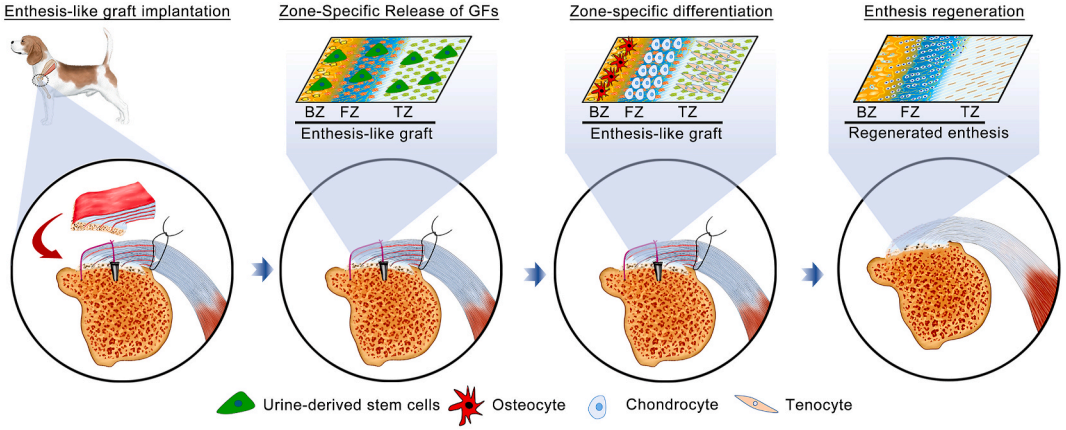

Fig. 9. Schematic illustration of the implantation of enthesis-like graft and its underlying mechanism on canine RC enthesis regeneration.

function of O-BDEM in RC enthesis regeneration. According to previous studies, direct protein incorporation is a widely and easily used strategy for GF introduction into a scaffold. However, these incorporated GFs released from scaffold in a burst pattern at the early stage, thus leading to several undesirable side-effects [26]. In addition, chemical cross-linking methods have been developed to incorporate GFs into a scaffold. However, the polymeric materials used for chemical cross-link would undoubtedly affect the structure and components of scaffold [28]. Meanwhile, some researchers incorporated GFs into a scaffold during production phase by microspheres or nanoparticles, which enables the synchronization of GFs release with scaffold degradation rate, realizing extended and/or sequential GFs release [29]. However, these methods are suitable for the 3D-printed scaffold fabricated with decellularized extracellular matrix ink [18], not suitable for extracellular matrix biomaterials derived from tissue or organ direct decellularization. Herein, we fused the CBP into the N-terminal of BMP-2, TGF-β3, or GDF-7 to synthesize three CBP-GFs capable of collagen binding. Our results showed that the O-BDEM zone-specifically adhered with the three CBP-GFs have the ability to sustained release BMP-2, TGF-β3 and GDF-7, thus presented superior inducibility in stimulating stem cells differentiate into osteocytes, chondrocytes, and tenocytes. Another advantage of CBP-GFs is that the fused CBP naturally exists in the blood, thus hard to be recognized by the immune system. This may be one of the reasons why CBP-GFs/O-BDEM has good biocompatibility *in-vivo*.

Clinically, high re-tear rate after RCT repair is the most common concern, which is largely attributed to inferior enthesis regeneration. Previous studies have shown that about half of surgically repaired RC healed with disorganized fibrovascular scar tissue instead of triphasic gradient enthesis [6,11]. Currently, many strategies have been developed to promote enthesis regeneration with scaffold- and/or cell-based strategies, which acquired satisfactory outcomes to some extent [2,77–81]. However, these strategies for treating RCT show variable in *in-vivo* performance [82–84]. In this study, we successfully fabricated a novel scaffold (CBP-GFs/O-BDEM), which not only directly replaced the damaged enthesis, due to high biomimicry and good biocompatibility, but also acted as a localized delivery system for the zone-specific release of BMP-2, TGF-β3, and GDF-7, inducing the interacted cells forming triphasic bone-fibrocartilage-tendon structure. Considering that endogenous cells are difficult to migrate into this large-size CBP-GFs/O-BDEM, we isolated cUSCs form canine urine and cultured on a temperature-responsive dishes to harvest autologous cUSC-sheets [36]. USCs have robust proliferation ability and multi-lineage differentiation, which can be accessed via a simple, non-invasive, and painless approach avoiding surgical procedures [39]. These advantages make it possible to use autologous USCs as seeding-cells for constructing an enthesis-like graft in this study or future clinical application. Additionally, using cell-sheet technique, we can implant stem cells largely without destroying the cell-cell contact, secreted ECM, and various bioactive substances formed during in-vitro culture. Thus, stem cells implanted in a cell-sheet manner showed a significantly better effect on tissue repair/regeneration than administering cells via direct seeding [79,85,86]. Using a preclinical canine model, our results determined that the ruptured infraspinatus tendon insertion patched with the enthesis-like graft presented better enhancement in healing quality compared with the direct suture, as characterized by improved formation of triphasic gradient enthesis and enhanced tensile resistance. This was not noted in the infraspinatus tendon healing site after augmentation repair with a porcine small intestine submucosa, acellular dermal matrix, or a poly--L-lactide device [87–89].

Several limitations still existed in our study. Firstly, in clinical setting, most of torn RC were chronical, and often associated with muscle atrophy, fatty infiltration and tendon retraction. While, in this study, an acute RC injury model was created to evaluate the function of our enthesis-like graft, and this model does not reflect the chronically torn RC. Future studies are expected to evaluate the potential of the enthesis-like graft as a bridging patch for chronic RC repair in the canine model. Secondly, the O-BDEM in this study was derived from canine NET. As for clinical translation, harvesting NET from human is the key issues to be solved first, and body donation or traumatic amputation may be suitable way for solving this issue. Thirdly, we only evaluated the *in-vivo* efficacy of the graft fabricated with CBP-GFs/O-BDEM and USC-sheets. Rigorously speaking, the O-BDEM, GFs/O-BDEM, CBP-GFs/O-BDEM, the graft fabricated with O-BDEM and USC-sheets, the graft fabricated with GFs/O-BDEM and USC-sheets should also be evaluated. In view that CBP-GFs/O-BDEM shows the best zone-specific inducibility on stem cell differentiation *in-vitro*, we did not set these groups in this study. This is more compliant with ethical requirements for laboratory animals. Fourthly, in this study, our enthesis-like graft was constructed by interleaving the CBP-GFs/O-BDEM with three cUSC-sheets and covering the surfaces of the CBP-GFs/O-BDEM with two cUSC-sheets. The drawbacks existing here are that the optimal cUSCs number implanted and the fate of the implanted USCs did not investigate. Owing to the harsh conditions of the injury site, part of cUSCs will die after implantation; thus, we enlarged the number of implanted cUSCs to ensure the efficacy in enthesis regeneration. As for the fate of the implanted USCs, based on our previous study [36], part of implanted cUSCs may differentiate into osteocytes, fibrochondrocytes, or tenocytes to participate enthesis regeneration *in-vivo*. Fifthly, our *in-vitro* results showed that the saturation binding amount of BMP-2, TGF-β3, and GDF-7 on DBM, DFM, and DTM is 8 μM, 6 μM, and 8 μM, respectively; thus, the concentrations were applied for constructing CBP-GFs/O-BDEM. However, only one CBP-GFs loading concentration was investigated. It will be meaningful to further optimize the CBP-GFs loading concentration to more effectively enhance enthesis regeneration.

5. Conclusion

In summary, this study described a detailed protocol for fabricating a novel scaffold (CBP-GFs/O-BDEM) that shows high similarity with native enthesis in morphology, composition and tensile resistance, at the same time, presents superior bioactivity in inducing the interacted stem cells down into osteogenic, chondrogenic and tenogenic lineages. CyTOF was successfully used to determine the low immunogenicity of CBP-GFs/O-BDEM at single-cell resolution using a mouse model. Meanwhile, autologous cUSC-sheets were interleaved into the page gaps of CBP-GFs/O-BDEM to bioengineer an enthesis-like graft, and its excellent performance on regenerating RC enthesis was determined in a canine model. This study indicates the enthesis-like graft may be an ideal strategy for patching large/massive RC tears in clinic and made significant breakthroughs in engineering graded interfacial tissue.

CRediT authorship contribution statement

Can Chen: Conceptualization, Formal analysis, Funding acquisition, Investigation, Project administration, Writing – original draft, Validation. **Qiang Shi:** Investigation, Methodology, Resources, Software, Visualization, Validation. **Muzhi Li:** Writing – review & editing, Methodology, Data curation, Software, Validation, Investigation, Methodology, Resources, Software, Visualization, Validation. **Yang Chen:** Investigation, Methodology, Resources, Software, Visualization, Validation. **Tao Zhang:** Investigation, Methodology, Resources, Software, Visualization, Validation. **Yan Xu:** Writing – review & editing, Methodology, Data curation, Software, Validation. **Shulin Ding:** Investigation, Methodology, Resources, Software, Visualization, Validation. **Zhanwen Wang:** Writing – review & editing, Methodology, Data curation, Software, Validation. **Xing Li:** Writing – review & editing, Methodology, Data curation, Software, Validation, Investigation, Methodology, Resources, Software, Visualization, Validation. **Chunfeng Zhao:** Supervision, Conceptualization, Writing – review & editing. **Lunquan Sun:** Supervision, Conceptualization, Writing – review & editing. **Jianzhong Hu:** Supervision, Conceptualization, Writing –

review & editing. **Hongbin Lu:** Conceptualization, Formal analysis, Funding acquisition, Investigation, Project administration.

Declaration of competing interest

The authors declare that they have no known competing financial interests or personal relationships that could have appeared to influence the work reported in this paper.

Acknowledgements

This work was supported by the National Natural Science Foundation of China (Nos. 81902192 and 81730068), the Science and Technology Major Project of Changsha (No. kh2003015), and the Postdoctoral Science Foundation of China (No. 2019M652809). Additionally, we thank the staffs at BL01B station of National Facility for Protein Science Shanghai and the BL15U1 station of the Shanghai Synchrotron Radiation Facility, Shanghai, China, for their kind assistance during the experiments.

Appendix A. Supplementary data

Supplementary data to this article can be found online at https://doi.org/10.1016/j.bioactmat.2021.12.021.

References

[1] S. Zhao, L. Peng, G. Xie, D. Li, J. Zhao, C. Ning, Effect of the interposition of calcium phosphate materials on tendon-bone healing during repair of chronic rotator cuff tear, Am. J. Sports Med. 42 (8) (2014) 1920–1929.
[2] G. Depres-Tremblay, A. Chevrier, M. Snow, M.B. Hurtig, S. Rodeo, M. D. Buschmann, Rotator cuff repair: a review of surgical techniques, animal models, and new technologies under development, J. Shoulder Elbow Surg. 25 (12) (2016) 2078–2085.
[3] S.T. Bianco, H.L. Moser, L.M. Galatz, A.H. Huang, Biologics and stem cell-based therapies for rotator cuff repair, Ann. N. Y. Acad. Sci. 1442 (1) (2019) 35–47.
[4] G. Criscenti, A. Longoni, A. Di Luca, C. De Maria, C.A. van Blitterswijk, G. Vozzi, L. Moroni, Triphasic scaffolds for the regeneration of the bone-ligament interface, Biofabrication 8 (1) (2016), 015009.
[5] H.H. Lu, S. Thomopoulos, Functional attachment of soft tissues to bone: development, healing, and tissue engineering, Annu. Rev. Biomed. Eng. 15 (2013) 201–226.
[6] K.A. Derwin, L.M. Galatz, A. Ratcliffe, S. Thomopoulos, Enthesis repair: challenges and opportunities for effective tendon-to-bone healing, J Bone Joint Surg Am 100 (16) (2018) e109.
[7] R.C. Mather 3rd, L. Koenig, D. Acevedo, T.M. Dall, P. Gallo, A. Romeo, J. Tongue, G. Williams Jr., The societal and economic value of rotator cuff repair, J Bone Joint Surg Am 95 (22) (2013) 1993–2000.
[8] P. Spennacchio, G. Banfi, D. Cucchi, R. D'Ambrosi, P. Cabitza, P. Randelli, Long-term outcome after arthroscopic rotator cuff treatment, Knee Surg. Sports Traumatol. Arthrosc. 23 (2) (2015) 523–529.
[9] E.J. Strauss, M.J. Salata, J. Kercher, J.U. Barker, K. McGill, B.R. Bach Jr., A. A. Romeo, N.N. Verma, Multimedia article. The arthroscopic management of partial-thickness rotator cuff tears: a systematic review of the literature, Arthroscopy 27 (4) (2011) 568–580.
[10] P.J. Millett, R.J. Warth, G.J. Dornan, J.T. Lee, U.J. Spiegl, Clinical and structural outcomes after arthroscopic single-row versus double-row rotator cuff repair: a systematic review and meta-analysis of level I randomized clinical trials, J. Shoulder Elbow Surg. 23 (4) (2014) 586–597.
[11] E.D. Bonnevie, R.L. Mauck, Physiology and engineering of the graded interfaces of musculoskeletal junctions, Annu. Rev. Biomed. Eng. 20 (2018) 403–429.
[12] A.J. Boys, M.C. McCorry, S. Rodeo, L.J. Bonassar, L.A. Estroff, Next generation tissue engineering of orthopedic soft tissue-to-bone interfaces, MRS Commun 7 (3) (2017) 289–308.
[13] S. Font Tellado, E.R. Balmayor, M. Van Griensven, Strategies to engineer tendon/ligament-to-bone interface: biomaterials, cells and growth factors, Adv. Drug Deliv. Rev. 94 (2015) 126–140.
[14] T. Lei, T. Zhang, W. Ju, X. Chen, B.C. Heng, W. Shen, Z. Yin, Biomimetic strategies for tendon/ligament-to-bone interface regeneration, Bioact Mater 6 (8) (2021) 2491–2510.
[15] F. Blaudez, S. Ivanovski, S. Hamlet, C. Vaquette, An overview of decellularisation techniques of native tissues and tissue engineered products for bone, ligament and tendon regeneration, Methods 171 (2020) 28–40.
[16] Q. Shi, Y. Chen, M. Li, T. Zhang, S. Ding, Y. Xu, J. Hu, C. Chen, H. Lu, Designing a novel vacuum aspiration system to decellularize large-size enthesis with preservation of physicochemical and biological properties, Ann. Transl. Med. 8 (21) (2020) 1364.
[17] M. Benjamin, D. McGonagle, Entheses: tendon and ligament attachment sites, Scand. J. Med. Sci. Sports 19 (4) (2009) 520–527.
[18] E. García-Gareta, Y. Abduldaiem, P. Sawadkar, C. Kyriakidis, F. Lali, K.V. Greco, Decellularised scaffolds: just a framework? Current knowledge and future directions, J. Tissue Eng. 11 (2020), 2041731420942903.
[19] H. Xiao, Y. Chen, M. Li, Q. Shi, Y. Xu, J. Hu, X. Li, C. Chen, H. Lu, Cell-free book-shaped decellularized tendon matrix graft capable of controlled release of BMP-12 to improve tendon healing in a rat model, Am. J. Sports Med. 49 (5) (2021) 1333–1347.
[20] C. Chen, F. Liu, Y. Tang, J. Qu, Y. Cao, C. Zheng, Y. Chen, M. Li, C. Zhao, L. Sun, J. Hu, H. Lu, Book-shaped acellular fibrocartilage scaffold with cell-loading capability and chondrogenic inducibility for tissue-engineered fibrocartilage and bone-tendon healing, ACS Appl. Mater. Interfaces 11 (3) (2019) 2891–2907.
[21] C. Chen, Y. Chen, M. Li, H. Xiao, Q. Shi, T. Zhang, X. Li, C. Zhao, J. Hu, H. Lu, Functional decellularized fibrocartilaginous matrix graft for rotator cuff enthesis regeneration: a novel technique to avoid in-vitro loading of cells, Biomaterials 250 (2020), 119996.
[22] A. Gilpin, Y. Yang, Decellularization strategies for regenerative medicine: from processing techniques to applications, BioMed Res. Int. 2017 (2017) 9831534.
[23] S.W. Linderman, R.H. Gelberman, S. Thomopoulos, H. Shen, Cell and biologic-based treatment of flexor tendon injuries, Operat. Tech. Orthop. 26 (3) (2016) 206–215.
[24] Y.H. Liao, Y.H. Chang, L.Y. Sung, K.C. Li, C.L. Yeh, T.C. Yen, S.M. Hwang, K.J. Lin, Y.C. Hu, Osteogenic differentiation of adipose-derived stem cells and calvarial defect repair using baculovirus-mediated co-expression of BMP-2 and miR-148b, Biomaterials 35 (18) (2014) 4901–4910.
[25] E. Augustyniak, T. Trzeciak, M. Richter, J. Kaczmarczyk, W. Suchorska, The role of growth factors in stem cell-directed chondrogenesis: a real hope for damaged cartilage regeneration, Int. Orthop. 39 (5) (2015) 995–1003.
[26] L. Deng, D. Li, Z. Yang, X. Xie, P. Kang, Repair of the calvarial defect in goat model using magnesium-doped porous hydroxyapatite combined with recombinant human bone morphogenetic protein-2, Bio Med. Mater. Eng. 28 (4) (2017) 361–377.
[27] W. Shen, X. Chen, J. Chen, Z. Yin, B.C. Heng, W. Chen, H.W. Ouyang, The effect of incorporation of exogenous stromal cell-derived factor-1 alpha within a knitted silk-collagen sponge scaffold on tendon regeneration, Biomaterials 31 (28) (2010) 7239–7249.
[28] A.J. Rufaihah, S.R. Vaibavi, M. Plotkin, J. Shen, V. Nithya, J. Wang, D. Seliktar, T. Kofidis, Enhanced infarct stabilization and neovascularization mediated by VEGF-loaded PEGylated fibrinogen hydrogel in a rodent myocardial infarction model, Biomaterials 34 (33) (2013) 8195–8202.
[29] M.A. Fernandez-Yague, S.A. Abbah, L. McNamara, D.I. Zeugolis, A. Pandit, M. J. Biggs, Biomimetic approaches in bone tissue engineering: integrating biological and physicomechanical strategies, Adv. Drug Deliv. Rev. 84 (2015) 1–29.
[30] M. Shahidi, Thrombosis and von Willebrand factor, Adv. Exp. Med. Biol. 906 (2017) 285–306.
[31] C. Dubois, L. Panicot-Dubois, G. Merrill-Skoloff, B. Furie, B.C. Furie, Glycoprotein VI-dependent and -independent pathways of thrombus formation in vivo, Blood 107 (10) (2006) 3902–3906.
[32] C. Addi, F. Murschel, G. De Crescenzo, Design and use of chimeric proteins containing a collagen-binding domain for wound healing and bone regeneration, Tissue Eng. B Rev. 23 (2) (2017) 163–182.
[33] M.L. Wong, L.G. Griffiths, Immunogenicity in xenogeneic scaffold generation: antigen removal vs. decellularization, Acta Biomater. 10 (5) (2014) 1806–1816.
[34] M. Orecchioni, D. Bedognetti, L. Newman, C. Fuoco, F. Spada, W. Hendrickx, F. M. Marincola, F. Sgarrella, A.F. Rodrigues, C. Ménard-Moyon, G. Cesareni, K. Kostarelos, A. Bianco, L.G. Delogu, Single-cell mass cytometry and transcriptome profiling reveal the impact of graphene on human immune cells, Nat. Commun. 8 (1) (2017) 1109.
[35] Z.C. Hao, S.Z. Wang, X.J. Zhang, J. Lu, Stem cell therapy: a promising biological strategy for tendon-bone healing after anterior cruciate ligament reconstruction, Cell Prolif 49 (2) (2016) 154–162.
[36] C. Chen, F. Liu, Y. Tang, J. Qu, Y. Cao, C. Zheng, Y. Chen, M. Li, C. Zhao, L. Sun, J. Hu, H. Lu, Book-Shaped Acellular Fibrocartilage Scaffold with Cell-Loading Capability and Chondrogenic Inducibility for Tissue-Engineered Fibrocartilage and Bone-Tendon Healing, ACS applied materials & interfaces, 2019.
[37] G. Bento, A.K. Shafigullina, A.A. Rizvanov, V.A. Sardao, M.P. Macedo, P. J. Oliveira, Urine-derived stem cells: applications in regenerative and predictive medicine, Cells 9 (3) (2020).
[38] X. Ji, M. Wang, F. Chen, J. Zhou, Urine-derived stem cells: the present and the future, Stem Cell. Int. 2017 (2017) 4378947.
[39] L. Chen, L. Li, F. Xing, J. Peng, K. Peng, Y. Wang, Z. Xiang, Human urine-derived stem cells: potential for cell-based therapy of cartilage defects, Stem Cell. Int. 2018 (2018) 4686259.
[40] Q. Liu, Y. Yu, R.L. Reisdorf, J. Qi, C.K. Lu, L.J. Berglund, P.C. Amadio, S.L. Moran, S.P. Steinmann, K.N. An, A. Gingery, C. Zhao, Engineered tendon-fibrocartilage-bone composite and bone marrow-derived mesenchymal stem cell sheet augmentation promotes rotator cuff healing in a non-weight-bearing canine model, Biomaterials 192 (2019) 189–198.
[41] Q. Liu, T. Hatta, J. Qi, H. Liu, A.R. Thoreson, P.C. Amadio, S.L. Moran, S. P. Steinmann, A. Gingery, C. Zhao, Novel engineered tendon-fibrocartilage-bone composite with cyclic tension for rotator cuff repair, J Tissue Eng Regen Med 12 (7) (2018) 1690–1701.
[42] R. Wilson, A.F. Diseberg, L. Gordon, S. Zivkovic, L. Tatarczuch, E.J. Mackie, J. J. Gorman, J.F. Bateman, Comprehensive profiling of cartilage extracellular matrix

formation and maturation using sequential extraction and label-free quantitative proteomics, Mol. Cell. Proteomics 9 (6) (2010) 1296–1313.
[43] M. Magrane, UniProt Knowledgebase: a Hub of Integrated Protein Data, Database (Oxford) 2011, 2011, p. bar009.
[44] M. Ashburner, C.A. Ball, J.A. Blake, D. Botstein, H. Butler, J.M. Cherry, A.P. Davis, K. Dolinski, S.S. Dwight, J.T. Eppig, M.A. Harris, D.P. Hill, L. Issel-Tarver, A. Kasarskis, S. Lewis, J.C. Matese, J.E. Richardson, M. Ringwald, G.M. Rubin, G. Sherlock, Gene ontology: tool for the unification of biology. The Gene Ontology Consortium, Nat. Genet. 25 (1) (2000) 25–29.
[45] H. Lu, C. Chen, Z. Wang, J. Qu, D. Xu, T. Wu, Y. Cao, J. Zhou, C. Zheng, J. Hu, Characterization of calcium and zinc spatial distributions at the fibrocartilage zone of bone–tendon junction by synchrotron radiation-based micro X-ray fluorescence analysis combined with backscattered electron imaging, Spectrochim. Acta B Atom Spectrosc. 111 (2015) 15–22.
[46] C.-Y. Chen, S.-S. Rao, L. Ren, X.-K. Hu, Y.-J. Tan, Y. Hu, J. Luo, Y.-W. Liu, H. Yin, J. Huang, J. Cao, Z.-X. Wang, Z.-Z. Liu, H.-M. Liu, S.-Y. Tang, R. Xu, H. Xie, Exosomal DMBT1 from human urine-derived stem cells facilitates diabetic wound repair by promoting angiogenesis, Theranostics 8 (6) (2018) 1607–1623.
[47] X. Zhang, W.-G. Guo, H. Cui, H.-Y. Liu, Y. Zhang, W.E.G. Müller, F.-Z. Cui, In vitroandin vivoenhancement of osteogenic capacity in a synthetic BMP-2 derived peptide-coated mineralized collagen composite, J. Tissue Eng.Regen. Med. 10 (2) (2016) 99–107.
[48] S. Agarwal, J.Y. Lee, Z. Zhou, P.J. Taub, M. Ramcharan, Y. Li, T. Akinbiyi, E. R. Maharam, D.J. Leong, D.M. Laudier, T. Ruike, P.J. Torina, M. Zaidi, R. J. Majeska, M.B. Schaffler, E.L. Flatow, H.B. Sun, BMP-12 treatment of adult mesenchymal stem cells in vitro augments tendon-like tissue formation and defect repair in vivo, PLoS One 6 (3) (2011).
[49] J. Chen, Y. Wang, C. Chen, C. Lian, T. Zhou, B. Gao, Z. Wu, C. Xu, Exogenous heparan sulfate enhances the TGF-β3-induced chondrogenesis in human mesenchymal stem cells by activating TGF-β/Smad signaling, Stem Cell. Int. 2016 (2016) 1–10.
[50] J. Sun, C. Mou, Q. Shi, B. Chen, X. Hou, W. Zhang, X. Li, Y. Zhuang, J. Shi, Y. Chen, J. Dai, Controlled release of collagen-binding SDF-1α from the collagen scaffold promoted tendon regeneration in a rat Achilles tendon defect model, Biomaterials 162 (2018) 22–33.
[51] C. Shi, W. Chen, B. Chen, T. Shan, W. Jia, X. Hou, L. Li, G. Ye, J. Dai, Bladder regeneration in a canine model using a bladder acellular matrix loaded with a collagen-binding bFGF, Biomaterials science 5 (12) (2017) 2427–2436.
[52] K. Sadtler, B.W. Allen, K. Estrellas, F. Housseau, D.M. Pardoll, J.H. Elisseeff, The scaffold immune microenvironment: biomaterial-mediated immune polarization in traumatic and nontraumatic Applications<sup/&gt, Tissue Eng Part A 23 (19–20) (2017) 1044–1053.
[53] S. Zhang, H. Li, H. Tao, H. Li, S. Cho, Y. Hua, J. Chen, S. Chen, Y. Li, Delayed early passive motion is harmless to shoulder rotator cuff healing in a rabbit model, Am. J. Sports Med. 41 (8) (2013) 1885–1892.
[54] K.A. Derwin, A.R. Baker, M.J. Codsi, J.P. Iannotti, Assessment of the canine model of rotator cuff injury and repair, J. Shoulder Elbow Surg. 16 (5) (2007) S140–S148.
[55] J. Ide, K. Kikukawa, J. Hirose, K. Iyama, H. Sakamoto, T. Fujimoto, H. Mizuta, The effect of a local application of fibroblast growth factor-2 on tendon-to-bone remodeling in rats with acute injury and repair of the supraspinatus tendon, J. Shoulder Elbow Surg. 18 (3) (2009) 391–398.
[56] S.A. Shah, I. Kormpakis, N. Havlioglu, M.S. Ominsky, L.M. Galatz, S. Thomopoulos, Sclerostin antibody treatment enhances rotator cuff tendon-to-bone healing in an animal model, J. Bone Joint Surg. 99 (10) (2017) 855–864.
[57] F.A. Barber, J.P. Burns, A. Deutsch, M.R. Labbe, R.B. Litchfield, A prospective, randomized evaluation of acellular human dermal matrix augmentation for arthroscopic rotator cuff repair, Arthroscopy 28 (1) (2012) 8–15.
[58] M.L. Williams, J.E. Holewinski, Use of a human acellular dermal wound matrix in patients with complex wounds and comorbidities, J. Wound Care 24 (6) (2015) 264–267, 261-2.
[59] P. Qiu, E.F. Simonds, S.C. Bendall, K.D. Gibbs Jr., R.V. Bruggner, M.D. Linderman, K. Sachs, G.P. Nolan, S.K. Plevritis, Extracting a cellular hierarchy from high-dimensional cytometry data with SPADE, Nat. Biotechnol. 29 (10) (2011) 886–891.
[60] A. Vishwakarma, N.S. Bhise, M.B. Evangelista, J. Rouwkema, M.R. Dokmeci, A. M. Ghaemmaghami, N.E. Vrana, A. Khademhosseini, Engineering immunomodulatory biomaterials to tune the inflammatory response, Trends Biotechnol. 34 (6) (2016) 470–482.
[61] A. Seidi, M. Ramalingam, I. Elloumi-Hannachi, S. Ostrovidov, A. Khademhosseini, Gradient biomaterials for soft-to-hard interface tissue engineering, Acta Biomater. 7 (4) (2011) 1441–1451.
[62] J.Z. Paxton, K. Donnelly, R.P. Keatch, K. Baar, Engineering the bone-ligament interface using polyethylene glycol diacrylate incorporated with hydroxyapatite, Tissue Eng Part A 15 (6) (2009) 1201–1209.
[63] Y. Cao, S. Yang, D. Zhao, Y. Li, S.S. Cheong, D. Han, Q. Li, Three-dimensional printed multiphasic scaffolds with stratified cell-laden gelatin methacrylate hydrogels for biomimetic tendon-to-bone interface engineering, J.Orthop. Translat 23 (2020) 89–100.
[64] R.A. Sun Han Chang, J.F. Shanley, M.E. Kersh, B.A.C. Harley, Tough and tunable scaffold-hydrogel composite biomaterial for soft-to-hard musculoskeletal tissue interfaces, Sci. Adv. 6 (34) (2020), eabb6763.
[65] C.W. Cheng, L.D. Solorio, E. Alsberg, Decellularized tissue and cell-derived extracellular matrices as scaffolds for orthopaedic tissue engineering, Biotechnol. Adv. 32 (2) (2014) 462–484.
[66] Yongchun Zhou, Shanshan Xie, Yifu Tang, Xiaoning Li, Yong Cao, Jianzhong Hu, Effect of book-shaped acellular tendon scaffold with bone marrow mesenchymal stem cells sheets on bone-tendon interface healing, J Orthop Translat 2426 (2020 Mar) 162–170.
[67] M. Su, Q. Zhang, Y. Zhu, S. Wang, J. Lv, J. Sun, P. Qiu, S. Fan, K. Jin, L. Chen, X. Lin, Preparation of Decellularized Triphasic Hierarchical Bone-Fibrocartilage-Tendon Composite Extracellular Matrix for Enthesis Regeneration, Advanced Healthcare Materials, 2019.
[68] F. Zhao, K. Xu, L.A. Kuntz, P. Foehr, K. Kuempel, A. Wagner, J. Tuebel, C. V. Deimling, R.H. Burgkart, Efficient decellularization for tissue engineering of the tendon-bone interface with preservation of biomechanics, PLoS One 12 (2) (2017).
[69] J.A. Bronstein, C.Y. Woon, S. Farnebo, A.W. Behn, T. Schmitt, H. Pham, A. B. Castillo, J. Chang, Physicochemical decellularization of composite flexor tendon-bone interface grafts, Plast. Reconstr. Surg. 132 (1) (2013) 94–102.
[70] T. Woods, P.F. Gratzer, Effectiveness of three extraction techniques in the development of a decellularized bone-anterior cruciate ligament-bone graft, Biomaterials 26 (35) (2005) 7339–7349.
[71] S. Farnebo, C.Y.L. Woon, J.A. Bronstein, T. Schmitt, D.P. Lindsey, H. Pham, A. B. Castillo, J. Chang, Decellularized tendon-bone composite grafts for extremity reconstruction, Plast. Reconstr. Surg. 133 (1) (2014) 79–89.
[72] S. Farnebo, C.Y. Woon, M. Kim, H. Pham, J. Chang, Reconstruction of the tendon-bone insertion with decellularized tendon-bone composite grafts: comparison with conventional repair, J. Hand Surg. 39 (1) (2014) 65–74.
[73] M. Bao, J. Xie, W.T.S. Huck, Recent advances in engineering the stem cell microniche in 3D, Adv. Sci. 5 (8) (2018).
[74] G. Abagnale, M. Steger, V.H. Nguyen, N. Hersch, A. Sechi, S. Joussen, B. Denecke, R. Merkel, B. Hoffmann, A. Dreser, U. Schnakenberg, A. Gillner, W. Wagner, Surface topography enhances differentiation of mesenchymal stem cells towards osteogenic and adipogenic lineages, Biomaterials 61 (2015) 316–326.
[75] Kamolrat Metavarayuth, Nanotopographical cues mediate osteogenesis of stem cells on virus substrates through BMP-2 intermediate, Nano Lett . (2019), https://doi.org/10.1021/acs.nanolett.9b02001.
[76] Xu Xue, Recent advances in design of functional biocompatible hydrogels for bone tissue engineering, Adv. Funct. Mater. (2021).
[77] W. Al-Hakim, A. Noorani, S. Lambert, Assessment and treatment strategies for rotator cuff tears, Shoulder Elbow 7 (2) (2015) 76–84.
[78] K. Atesok, F.H. Fu, M.R. Wolf, M. Ochi, L.M. Jazrawi, M.N. Doral, J.H. Lubowitz, S. A. Rodeo, Augmentation of tendon-to-bone healing, J Bone Joint Surg Am 96 (6) (2014) 513–521.
[79] Y. Harada, Y. Mifune, A. Inui, R. Sakata, T. Muto, F. Takase, Y. Ueda, T. Kataoka, T. Kokubu, R. Kuroda, M. Kurosaka, Rotator cuff repair using cell sheets derived from human rotator cuff in a rat model, J. Orthop. Res. 35 (2) (2017) 289–296.
[80] C. Zheng, H. Lu, Y. Tang, Z. Wang, H. Ma, H. Li, H. Chen, Y. Chen, C. Chen, Autologous freeze-dried, platelet-rich plasma carrying icariin enhances bone-tendon healing in a rabbit model, Am. J. Sports Med. 47 (8) (2019) 1964–1974.
[81] J. Hu, J. Qu, D. Xu, T. Zhang, L. Qin, H. Lu, Combined application of low-intensity pulsed ultrasound and functional electrical stimulation accelerates bone-tendon junction healing in a rabbit model, J. Orthop. Res. 32 (2) (2014) 204–209.
[82] L.V. Gulotta, D. Kovacevic, J.R. Ehteshami, E. Dagher, J.D. Packer, S.A. Rodeo, Application of bone marrow-derived mesenchymal stem cells in a rotator cuff repair model, Am. J. Sports Med. 37 (11) (2009) 2126–2133.
[83] R.M. Degen, A. Carbone, C. Carballo, J. Zong, T. Chen, A. Lebaschi, L. Ying, X. H. Deng, S.A. Rodeo, The effect of purified human bone marrow-derived mesenchymal stem cells on rotator cuff tendon healing in an athymic rat, Arthroscopy 32 (12) (2016) 2435–2443.
[84] S. Yokoya, Y. Mochizuki, K. Natsu, H. Omae, Y. Nagata, M. Ochi, Rotator cuff regeneration using a bioabsorbable material with bone marrow-derived mesenchymal stem cells in a rabbit model, Am. J. Sports Med. 40 (6) (2012) 1259–1268.
[85] J. Yang, M. Yamato, C. Kohno, A. Nishimoto, H. Sekine, F. Fukai, T. Okano, Cell sheet engineering: recreating tissues without biodegradable scaffolds, Biomaterials 26 (33) (2005) 6415–6422.
[86] P.Y. Neo, T.K. Teh, A.S. Tay, M.C. Asuncion, S.N. Png, S.L. Toh, J.C. Goh, Stem cell-derived cell-sheets for connective tissue engineering, Connect. Tissue Res. 57 (6) (2016) 428–442.
[87] L.M. Dejardin, S.P. Arnoczky, B.J. Ewers, R.C. Haut, R.B. Clarke, Tissue-engineered rotator cuff tendon using porcine small intestine submucosa. Histologic and mechanical evaluation in dogs, Am. J. Sports Med. 29 (2) (2001) 175–184.
[88] K.A. Derwin, M.J. Codsi, R.A. Milks, A.R. Baker, J.A. McCarron, J.P. Iannotti, Rotator cuff repair augmentation in a canine model with use of a woven poly-L-lactide device, J. Bone Jt. Surg. Am. 91 (5) (2009) 1159–1171.
[89] J.E. Adams, M.E. Zobitz, J.S. Reach, K.-N. An, S.P. Steinmann, Rotator cuff repair using an acellular dermal matrix graft: an in vivo study in a canine model, arthroscopy, J. Arthrosc. Relat. Surg. 22 (7) (2006) 700–709.